Sequences for controlling laser excitation with femtosecond three-pulse four-wave mixing

Igor Pastirk,† Emily J. Brown, Bruna I. Grimberg, Vadim V. Lozovoy‡ and Marcos Dantus*

Department of Chemistry, Michigan State University, East Lansing, MI 48824-1332, USA. E-mail: dantus@cem.msu.edu

Received 30th March 1999

Three-pulse four-wave mixing (FWM) is used here to study and control laser excitation processes. For general laser excitation processes, after a molecule interacts resonantly with a laser pulse, the molecule has a probability of being in the ground or in the excited state. Control over this process depends on the phase and amplitude of the electric fields that interact with the molecular system. Here we show how three-pulse FWM can be used to control the excitation of iodine molecules. Depending on the time delay between the first two pulses, the observed signal reflects the dynamics of the ground or excited state. A theoretical formalism based on the density matrix formulation is presented and solved for a four-level system. Experiments are found to be in excellent agreement with the theory. The influence of linear chirp on three-pulse FWM experiments is explored. Spectrally dispersed three-pulse FWM is found to be extremely useful for studying the effect of chirp on laser excitation of molecular systems. Experimental demonstrations of these effects are included.

1. Introduction

Three-pulse four-wave mixing (FWM) is a nonlinear spectroscopic method that combines the interaction of three laser pulses in a phase-matched geometry with a well-defined time sequence of the pulses. The signal from these measurements arises from a third-order polarization resulting from the interaction of the three electric fields and is itself a coherent beam corresponding to a fourth electromagnetic wave. Various groups have used this technique to study the dynamics of molecules in the condensed phase.[1–3] Three-pulse FWM is similar to the pump–probe technique in that a preparation step is followed, after some variable time delay, by a probing step.[4] However, three-pulse FWM allows for a greater degree of control over the preparation and probing processes. Here we present this technique as an ideal tool to learn about and manipulate the quantum mechanical processes involved in laser control of chemical reactions. We present a theoretical formalism that reveals which 'knobs' are available for controlling laser–molecule interactions.

† Affiliated with the Institute for Nuclear Sciences "VINCA", Belgrade, F. R. Yugoslavia.
‡ Permanent address: N. N. Semenov Institute of Chemical Physics, RAS, Moscow, Russia.

Experimental demonstration of control using two different pulse sequences is included in addition to an exploration of the effects of laser chirp in three-pulse FWM experiments.

A two-level system is the ideal starting point for discussing laser excitation. The probability of excitation from the ground to the excited state in a two-level system is expressed quantum mechanically as $|\langle e|\boldsymbol{\mu}\cdot\boldsymbol{E}(t)|g\rangle|^2 = \langle e|\boldsymbol{\mu}\cdot\boldsymbol{E}(t)|g\rangle\langle g|\boldsymbol{\mu}\cdot\boldsymbol{E}(t)^*|e\rangle$, where $\boldsymbol{\mu}$ is the transition dipole and $\boldsymbol{E}(t)$ is the electric field. This expression implies that two interactions with the electric field are required, one with $\boldsymbol{E}(t)$ and one with $\boldsymbol{E}(t)^*$, to transfer part of the population from one state to the other. The excitation process, as measured in all linear spectroscopy methods, is a good example of this type of population transfer. Although both interactions are with the same field for a general excitation process, the two interactions do not imply that it is a two-photon process. The possibilities for influencing the excitation process with a simple laser pulse are minimal. However, if one had individual control over each of the electric fields involved in the excitation, full control could be achieved. Therefore, a technique that allows individual manipulation of the electric fields $\boldsymbol{E}(t)$ and $\boldsymbol{E}(t)^*$, such as three-pulse FWM, can be used to gain control over the transfer of population between the ground and the excited states.[5]

In the past decade, we have witnessed tremendous progress in the experimental demonstration of laser control of chemical reactions. This area of research has been reviewed recently.[6,7] Here we briefly mention the key principles for some of the most salient techniques. "Coherent control" depends on the quantum mechanical interference between two excitation paths created by two phase-locked lasers. Often the experiments are carried out by picking two lasers that can reach the same quantum mechanical state by one-, two-, or three-photon transitions. This technique is typically formulated in the frequency domain with phase as the controlling knob. The "pump–dump" technique involves the transfer of population between two or more states; control is achieved by taking advantage of the dynamics of the molecular system. This technique is typically formulated in the time domain. The time between the pulses is the control knob; therefore, most pump–probe experiments in the femtosecond time scale can be considered examples of this technique. "Mode-selective control" involves using one pulse to select a vibrational overtone of the molecule and a second pulse to cleave the bond that has been selectively excited. This technique combines frequency and time resolution (usually in nanoseconds). "Quantum control" usually involves a single laser pulse that is tailored in the time and frequency domains. Typically the control knobs are linear chirp, pulse duration (transform-limited pulses), and pulse intensity. Experimental demonstrations of this technique often involve multiphoton transitions. "Optimal control" seeks to find the optimal electric field to cause the desired excitation. Theoretically, this search can be carried out by two approaches. The first is to seek a direct solution of the quantum mechanical problem for the optimal field (a problem that is computationally feasible for very simple systems). The second is to use an algorithm that quickly explores different possible fields and contains a feedback on the degree of success that each field attains. Experimentally, groups have demonstrated equipment that can be used to search for the 'ideal' laser pulse to achieve a particular outcome. This method has been demonstrated recently to control a laser-initiated chemical reaction.[8]

It is clear from this brief overview that laser control of chemical reactions depends on the repeated interaction between the laser fields and molecules in the system. Although there are various formulations of the problem, the fundamental goal is to control population transfer to different quantum states (leading to different products of chemical reactions) by tailoring the electric fields in the time and frequency domains. In this paper, we use three-pulse FWM to study this process closely. We demonstrate how three-pulse FWM can be used to understand laser excitation, to predict the outcome from simple pulse sequences, and to achieve experimental control over the population transfer between two states. The role of linear chirp is also explored experimentally to show its effect on the dynamics of the system.

A quantum mechanical description of three-pulse FWM is given to illustrate the different experiments that become available for controlling population transfer when using different pulse sequences. This description is given in terms of the density matrix, a formalism that is ideal for the understanding of nonlinear spectroscopy.[9,10] Of particular importance is that this description allows one to follow the independent interactions of the system with the electric fields and does not force one into thinking only of absorption or emission of a photon. One of the most important aspects of this formalism is that one can see why two fields are required to transfer population, as discussed earlier. One can also explore what is the nature of the *coherence* formed after a

single electric field interaction with the system. These aspects are discussed in terms of the explicit solution for a two-level system. By solving the quantum mechanical equations of a four-level system that includes two vibrational levels for both the ground and excited states, we show that the time evolution of the system between the first and second electric field interactions can be used to control the population transfer. We further demonstrate how to control the excitation process in a molecule.

Molecular iodine is used here as a model system to demonstrate both theoretical and experimental control over the population transfer using three-pulse FWM. Depending on the precise timing between the laser pulses, we can control the contribution of the ground or the excited state. In both cases, the impulsive excitation of multiple vibrational and rotational levels by the femtosecond laser pulses leads to the observation of wavepacket dynamics characteristic of molecular iodine in the ground or the excited state. For these experiments, the molecular dynamics of the system play an important role in the control of population transfer between ground and excited states. Quantum simulations based on a four-level system are in excellent agreement with the experimental data.

In addition to exploring the effect of different pulse sequences, we have also explored the effect of linearly chirped electric fields on three-pulse FWM measurements. Chirped pulses affect the phase of the individual contributions from rovibrational levels of the molecular system. These effects are followed in time and the data show different dephasing dynamics depending on the magnitude and sign of the chirp. These effects are also observed by spectrally dispersing the three-pulse FWM signal to measure the phase-dependent amplitude of each of the different spectral components. This method, spectrally dispersed three-pulse FWM, is ideal for characterizing and understanding molecular excitation with chirped laser fields.[11]

This paper is organized as follows. A theoretical description of three-pulse FWM is given first in Section 2. The description begins with a discussion that illustrates, with double-sided Feynman diagrams, the various processes that are accessible depending on the relative timing of the three electric fields and quantum mechanical expressions involving the density matrix solution of two-level and four-level systems. Section 3 describes the experimental set-up. Section 4 presents the experimental results and examines them in terms of the theoretical background given in Section 2. Excellent agreement between theory and experiment is shown. The role of chirped laser fields is explored by three-pulse FWM and spectrally dispersed three-pulse FWM. Finally, Section 5 uses the conclusions from the experimental results and discussion to examine the application of this technique to understand and achieve laser control of chemical reactions.

2. Theory

The purpose of this section is to introduce a formalism that gives a theoretical foundation to our observations. A more complete treatment of transient grating techniques, double-sided Feynman diagrams, and a review of related work can be found in a previous publication from our group.[12] Before we focus on solving the density matrix for our system, we briefly summarize the important points of the four-wave mixing set-up and collection that we used for the experiments presented in Section 4.

Many possible four-wave mixing (FWM) signals can be formed in the forward box configuration; however, each one has a unique wave vector determined by the phase-matching geometry. The signal detected at the lower right corner of the box is identified by the wave vector $\boldsymbol{k}_s = \boldsymbol{k}_a - \boldsymbol{k}_b + \boldsymbol{k}_c$ and is the one described in this paper (see Fig. 1). We have explored two different pulse sequences here; in pulse sequence I (PS-I), fields E_a and E_b precede E_c, and in pulse sequence II (PS-II), field E_c precedes E_b and E_a. (See the top of Figs. 2 and 3 for schematic diagrams of the pulse sequences.) For some of the measurements, E_a and E_b are separated by a fixed time delay (τ_{ab}) while E_c is scanned in time (τ). In other measurements, E_a and E_b are coincident in time ($\tau_{ab} = 0$) and E_c is scanned. In the forward box geometry, field E_a and E_c are equivalent. This implies that the only difference between PS-I and PS-II is that for PS-I the first time delay (τ_{ab}) is fixed and the second one (τ) is variable. For PS-II, the first time delay (τ) is variable and the second one (τ_{ab}) is fixed. Also notice that in PS-I, field E_a precedes E_b for $\tau_{ab} > 0$; in PS-II, field E_b precedes E_a for $\tau_{ab} > 0$. We have explored other sequences; results from these studies will be published elsewhere.[13]

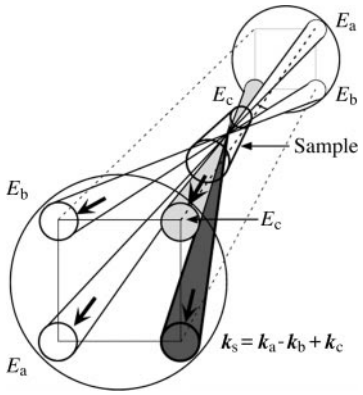

Fig. 1 Forward box configuration for the three-pulse FWM experiments. The three laser fields are overlapped spatially in the sample and arranged temporarily in a given pulse sequence. The three-pulse FWM signal is detected in direction represented by wave vector $\boldsymbol{k}_s$.

2.1. Double-sided Feynman diagrams

Double-sided Feynman diagrams provide a graphical tool to interpret the observation of ground and excited state dynamics from the FWM signal. Please see refs. 9, 10, and 14 for more extensive details than what is given here on the use of Feynman diagrams for understanding nonlinear spectroscopy. Under the rotating wave approximation, there are eight possible diagrams to describe the signal obtained with our experimental set-up; four are applicable to PS-I while only two apply to PS-II, as shown in Figs. 2 and 3. (See ref. 12 for more complete details on the eight diagrams.) The Feynman diagrams demonstrate how the density matrix operator $\hat{\rho}$ changes with the electric field interactions (wavy arrows) as a function of time. Dipole interactions with $E_j \exp(-i\omega_j t + i\boldsymbol{k}_j \cdot \boldsymbol{r})$ are shown as right-pointing arrows while left-pointing arrows correspond to $E_j^* \exp(i\omega_j t - i\boldsymbol{k}_j \cdot \boldsymbol{r})$ where j = a, b, or c. The first term in the exponent of these expressions, $(\pm i\omega_j t)$, along with the nature of the bra and ket determine whether the arrows indicate absorption or emission processes. Arrows pointing toward the center of the diagram are associated with the photon annihilation operator while those directed away from the center are associated with the photon creation operator.[10] The particular phase-matching configuration chosen determines the sign of the individual wave vectors for the three incoming fields. In our case ($\boldsymbol{k}_s = \boldsymbol{k}_a - \boldsymbol{k}_b + \boldsymbol{k}_c$), fields E_a and E_c must point right ($+\boldsymbol{k}_j$) and E_b points left ($-\boldsymbol{k}_j$).

The intensity of the FWM signal, $I_{FWM}(\tau_{ab}, \tau)$, depends on the time-dependent third-order polarization, $P^{(3)}(\boldsymbol{k}_s, t)$ according to[9,10,15]

$$I_{FWM}(\tau_{ab}, \tau) \propto \int_{-\infty}^{\infty} |P^{(3)}(\boldsymbol{k}_s, t)|^2 \, dt \tag{1}$$

for homodyne detection. This time-dependent third-order polarization is specific for a given phase-matching condition. For a molecular ensemble $P^{(3)}(\boldsymbol{k}_s, t)$ is defined as

$$P^{(3)}(\boldsymbol{k}_s, t) = \mathrm{Tr}[\hat{P}\hat{\rho}_s^{(3)}(t)] \tag{2}$$

where $\hat{P}$ is the polarization operator and $\hat{\rho}_s^{(3)}$ is the third-order density operator in the direction of the signal. Using double-sided Feynman diagrams (see Figs. 2 and 3), the temporal evolution of $\hat{\rho}$ can be analyzed by examining all the possible interactions of the electric fields on the sample.

We assume near-resonant excitation between the ground and excited states, labeled g and e respectively, for the Feynman diagrams shown in Figs. 2 and 3. The relative vertical position of the arrows and the labels t_1, t_2 and t_3 give the time order of each field. The emission of the signal field from the ket side has not been shown in order to simplify the diagrams in both figures. The symbols g, g′, e and e′ on the ket and bra sides of the diagram represent different rovibrational levels in each electronic state. An electric field interaction occurs on either the bra or the ket, but

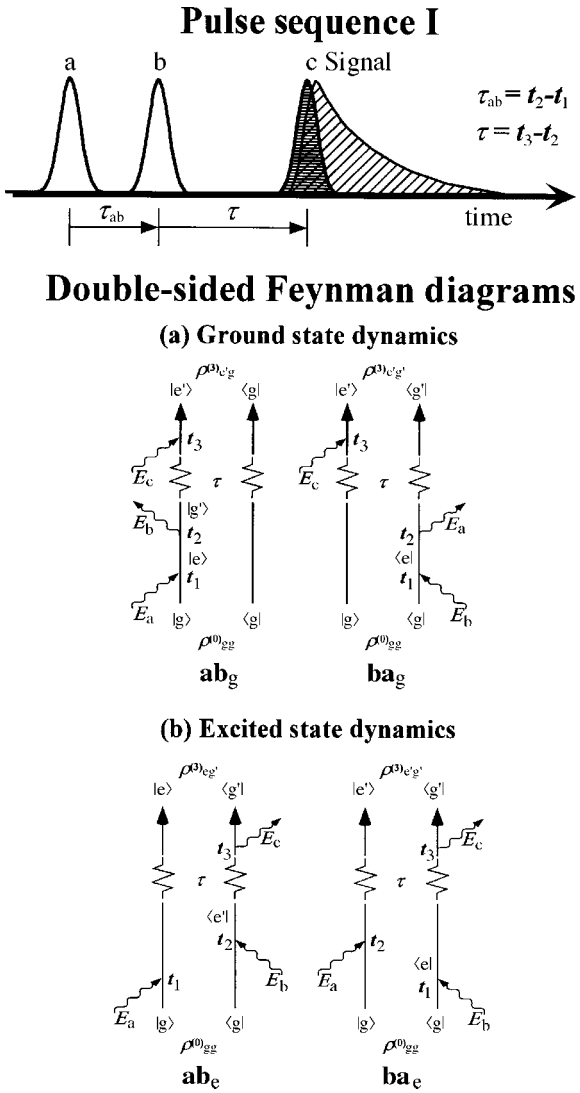

Fig. 2 Double-sided Feynman diagrams corresponding to PS-I shown at the top for the three-pulse FWM process. τ_{ab} is a fixed time delay between fields E_a and E_b and τ is a variable time delay between fields E_b and E_c. (a) Diagrams representing the observation of ground state dynamics. When fields E_a and E_b coincide in time, both diagrams contribute to the signal, but when E_a precedes E_b, only the diagram on the left side describes the process. (b) Diagrams depicting the observation of excited state dynamics. For $\tau_{ab} = 0$, both diagrams contribute to observed dynamics, while for τ_{ab} greater than the pulse duration, only $\mathbf{ab_e}$ applies.

not on both. Thus, when only one electric field interacts with the system, a change occurs on only one side of the Feynman diagram (bra or ket) giving rise to a polarization.

The choice of the spectroscopic technique used to analyze the non-linear optical measurements depends on the nature of the applied electric fields. For time-resolved measurements, the polarization is obtained from the density matrix, $\hat{\rho}^{(n)}(t)$, after the interaction with n electric fields in the time domain. For frequency-resolved measurements, the polarization is proportional to $\hat{\rho}^{(n)}(\Omega)$ in the frequency domain. The polarization of the molecular system can be defined as $P^{(n)}(r, t) = \chi^{(n)}(\Omega)E_s$ where E_s is the electric field that corresponds to the FWM signal.[10] In this case, the polarization is proportional to the susceptibility of the molecular system. Thus, in diagram $\mathbf{ab_g}$ in Fig. 2a, the transformation of $\rho^{(0)}_{gg}$ to $\rho^{(1)}_{eg}$ when field E_a acts on the ket at time t_1 contributes to the

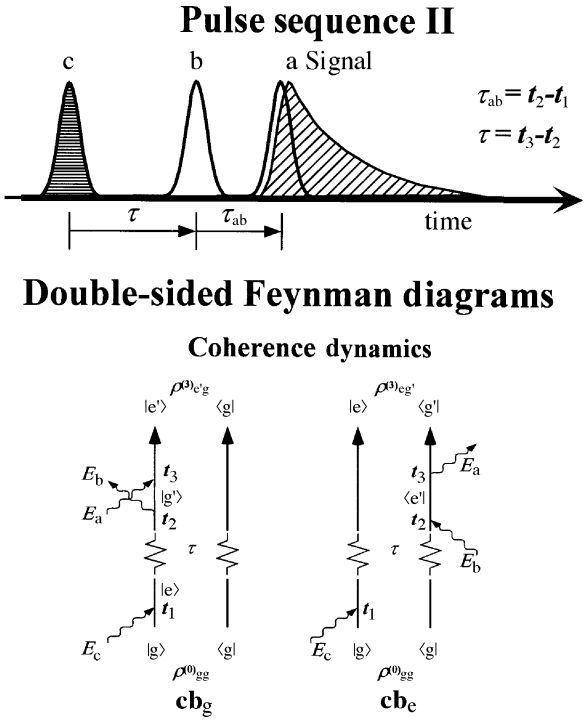

Fig. 3 Double-sided Feynman diagrams corresponding to PS-II shown at the top for the three-pulse FWM process. τ is a variable time delay between fields E_c and E_b and τ_{ab} is a fixed time delay between fields E_b and E_a. These diagrams describe the processes for the observation of coherence dynamics between ground and exited states. Both diagrams apply for $\tau_{ab} \geqslant 0$.

susceptibility according to $\langle e|\boldsymbol{\mu}\cdot\boldsymbol{E}_a(t-t_1)|g\rangle/(\Omega_{eg}-\omega_a)$ where $\Omega_{eg}=(E_e-E_g)/\hbar=-\Omega_{ge}$ and E_e and E_g are the energies of the excited and ground states, respectively. The entire interaction sequence and the transformation of $\hat{\rho}$ in diagram $\mathbf{ab}_g$ is

$$\rho^{(0)}_{gg} \xrightarrow{E_a(t)} \rho^{(1)}_{eg} \xrightarrow{E_b(t)} \rho^{(2)}_{g'g} \xrightarrow{E_c(t)} \rho^{(3)}_{e'g} ;$$

these three laser field interactions give a contribution to the nonlinear susceptibility as[14]

$$\chi^{(3)}_{ab_g} \propto N \sum_{gg',ee'} \rho^{(0)}_{gg} \frac{\langle g|\boldsymbol{\mu}\cdot\boldsymbol{e}_s^*|e'\rangle\langle e'|\boldsymbol{\mu}\cdot\boldsymbol{e}_c|g'\rangle\langle g'|\boldsymbol{\mu}\cdot\boldsymbol{e}_b^*|e\rangle\langle e|\boldsymbol{\mu}\cdot\boldsymbol{e}_a|g\rangle}{(\Omega_{eg}-\omega_a)(\Omega_{g'g}-\omega_a+\omega_b)(\Omega_{e'g}-\omega_a+\omega_b-\omega_c)} \tag{3}$$

where $\boldsymbol{e}_i$ is the polarization unit vector corresponding to $\boldsymbol{E}_i(t)$. Table 1 shows the corresponding expressions for the nonlinear susceptibilities for each of the other double-sided Feynman diagrams in Figs. 2 and 3. These expressions are included here to conceptually illustrate the meaning of each of the diagrams in Figs. 2 and 3. However, these formulae, which are usually used for frequency-resolved techniques, are not used to derive the formalism used to simulate our time-resolved experiments (*vide infra*).

Fig. 2(a) shows two of the applicable Feynman diagrams for PS-I when $\tau_{ab}=0$. The FWM processes represented by these two double-sided Feynman diagrams result in the observation of ground state dynamics. In these cases, a transient grating is formed in the ground state $\rho^{(2)}_{g'g}(t)$ and $\rho^{(2)}_{gg'}(t)$ by fields E_a and E_b. Field E_c induces a polarization after a time delay τ, indicated by a break in the time arrows, and the signal beam emitted by this polarization reveals ground state dynamics information. Two different diagrams describe this observation because the sequence between fields E_a and E_b is not defined. When fields E_a and E_b are separated in time, the sequence of the pulses better defines each process. For example, in Fig. 2(a), field E_a precedes field E_b in the diagram shown on the left side, while field E_b precedes field E_a in the diagram on the right side.

Table 1 Nonlinear susceptibilities corresponding to the double-sided Feynman diagrams in Figs. 2 and 3

$$\chi^{(3)}_{\mathbf{ba}_g} \propto N \sum_{gg',ee'} \rho^{(0)}_{gg} \frac{\langle g'|\boldsymbol{\mu}\cdot\boldsymbol{e}^*_s|e'\rangle\langle e'|\boldsymbol{\mu}\cdot\boldsymbol{e}_c|g\rangle\langle e|\boldsymbol{\mu}\cdot\boldsymbol{e}_a|g'\rangle\langle g|\boldsymbol{\mu}\cdot\boldsymbol{e}^*_b|e\rangle}{(\Omega_{ge}+\omega_b)(\Omega_{gg'}-\omega_a+\omega_b)(\Omega_{e'g'}-\omega_a+\omega_b-\omega_c)}$$

$$\chi^{(3)}_{\mathbf{ab}_e} \propto N \sum_{gg',ee'} \rho^{(0)}_{gg} \frac{\langle g'|\boldsymbol{\mu}\cdot\boldsymbol{e}^*_s|e\rangle\langle e'|\boldsymbol{\mu}\cdot\boldsymbol{e}_c|g'\rangle\langle g|\boldsymbol{\mu}\cdot\boldsymbol{e}^*_b|e'\rangle\langle e|\boldsymbol{\mu}\cdot\boldsymbol{e}_a|g\rangle}{(\Omega_{eg}-\omega_a)(\Omega_{ee'}-\omega_a+\omega_b)(\Omega_{eg'}-\omega_a+\omega_b-\omega_c)}$$

$$\chi^{(3)}_{\mathbf{ba}_e} \propto N \sum_{gg',ee'} \rho^{(0)}_{gg} \frac{\langle g'|\boldsymbol{\mu}\cdot\boldsymbol{e}^*_s|e'\rangle\langle e|\boldsymbol{\mu}\cdot\boldsymbol{e}_c|g'\rangle\langle e'|\boldsymbol{\mu}\cdot\boldsymbol{e}_a|g\rangle\langle g|\boldsymbol{\mu}\cdot\boldsymbol{e}^*_b|e\rangle}{(\Omega_{ge}+\omega_b)(\Omega_{e'e}-\omega_a+\omega_b)(\Omega_{e'g'}-\omega_a+\omega_b-\omega_c)}$$

$$\chi^{(3)}_{\mathbf{cb}_g} \propto N \sum_{gg',ee'} \rho^{(0)}_{gg} \frac{\langle g|\boldsymbol{\mu}\cdot\boldsymbol{e}^*_s|e'\rangle\langle e'|\boldsymbol{\mu}\cdot\boldsymbol{e}_a|g'\rangle\langle g'|\boldsymbol{\mu}\cdot\boldsymbol{e}^*_b|e\rangle\langle e|\boldsymbol{\mu}\cdot\boldsymbol{e}_c|g\rangle}{(\Omega_{eg}-\omega_c)(\Omega_{g'g}-\omega_c+\omega_b)(\Omega_{e'g}-\omega_c+\omega_b-\omega_a)}$$

$$\chi^{(3)}_{\mathbf{cb}_e} \propto N \sum_{gg',ee'} \rho^{(0)}_{gg} \frac{\langle g'|\boldsymbol{\mu}\cdot\boldsymbol{e}^*_s|e\rangle\langle e'|\boldsymbol{\mu}\cdot\boldsymbol{e}_a|g'\rangle\langle g|\boldsymbol{\mu}\cdot\boldsymbol{e}^*_b|e'\rangle\langle e|\boldsymbol{\mu}\cdot\boldsymbol{e}_c|g\rangle}{(\Omega_{eg}-\omega_c)(\Omega_{ee'}-\omega_c+\omega_b)(\Omega_{eg'}-\omega_c+\omega_b-\omega_a)}$$

Thus, when τ_{ab} is greater than the pulse duration of the laser, only the left Feynman diagram ($\mathbf{ab}_g$) applies (see the pulse sequence at top of Fig. 2).

The Feynman diagrams representing the four-wave mixing processes responsible for the observation of excited state dynamics for **PS-I** are shown in Fig. 2(b). In addition to the near-resonance requirement, the excited state must be long-lived with respect to the pulse duration of the laser in order to observe the excited state dynamics. This condition is clearly satisfied here. The transient grating is formed in the excited state $\rho^{(2)}_{ee}(t)$ and $\rho^{(2)}_{e'e}(t)$ by fields E_a and E_b. This time the signal beam resulting from the polarization induced by E_c after a time delay τ reveals excited state dynamics. Again both diagrams contribute for $\tau_{ab} = 0$, but only $\mathbf{ab}_e$ contributes to the signal for τ_{ab} is larger than the pulse duration. In the following sections (2.3 and 2.4), we will show that the time delay τ_{ab} can be used to discriminate among the processes that lead to the observation of ground state or excited state dynamics. Therefore, *in addition* to sorting between the different field interactions (*i.e.* selecting right- or left-side Feynman diagrams), the proper choice of the time delay τ_{ab} can separate the observation of ground and excited state dynamics (*i.e.* selecting either the top or bottom left-side Feynman diagram in Fig. 2).

The Feynman diagrams in Fig. 3 depict the observation of signal when field E_c precedes E_b and E_a in **PS-II**. After the first field E_c interacts with the system, a coherence $\rho^{(1)}_{eg}(t)$ is generated between the ground and excited states. After time delay τ, field E_b interacts with the system resulting in the formation of a transient grating in either the ground $\rho^{(2)}_{g'g}(t)$ or excited $\rho^{(2)}_{ee'}(t)$ state. The signal is created when E_a induces a polarization after time τ_{ab} following the formation of the transient grating. Unlike **PS-I** measurements where the signal reveals the population dynamics in the ground or excited states, **PS-II** measurements reveal an electronic coherence between the ground and excited states. Note that both $\mathbf{cb}_g$ and $\mathbf{cb}_e$ diagrams apply for $\tau_{ab} \geqslant 0$.

2.2. Density matrix

The FWM signal depends on the square of the electric field generated by the three incident electric fields.[10,16] As shown earlier in eqn. (1), in order to derive the signal in the weak interaction limit, we need to calculate the quantum average value of the polarization in third-order perturbation theory. After an odd number of applied pulses, the density matrix represents a coherence between the ground and the excited states, ρ_{ge} or ρ_{eg} (see Fig. 2). After an even number of applied pulses, the density matrix represents the population of the ground and excited states, diagonal terms ρ_{gg} or ρ_{ee}, and rovibrational coherence terms in both the ground and excited states $\rho_{gg'}$ and $\rho_{ee'}$. The derivation of the propagation of the density matrix is based on the Liouville space formulation. The purpose of the following sections is to analytically show the control mechanism and its dependence on the control parameter τ_{ab} and on the variable time delay τ. As a first step we will make the derivation for a two-level system, which is a tractable system and shows the source of the control mechanism. We extend the calculation to a four-level system following the two-level formulation.

2.3. Two-level system

The theoretical formalism derived below is for the PS-I case. A description of how to modify the final equations that correspond to PS-II will be given in Section 4. The notation for the interacting fields will correspond to the order in which they are applied; thus for PS-I, a = 1, b = 2, and c = 3. The density matrix of a system of two levels, $|g\rangle = |1\rangle$ and $|e\rangle = |2\rangle$, at initial time t_0 is given by

$$\hat{\rho}(t_0) = \begin{pmatrix} \rho_{11} & \rho_{12} \\ \rho_{21} & \rho_{22} \end{pmatrix} = \begin{pmatrix} 1 & 0 \\ 0 & 0 \end{pmatrix} \tag{4}$$

where $\rho_{11} = 1$ because all the population is in the ground state. The perturbation solution of the density matrix equation of motion for weak dipole interactions with successive n electric fields is based on the expansion of the density matrix,

$$\hat{\rho} = \hat{\rho}^{(0)} + \hat{\rho}^{(1)}(t) + \hat{\rho}^{(2)}(t) + \hat{\rho}^{(3)}(t) \cdots + \hat{\rho}^{(n)}(t) \quad \text{and} \tag{5}$$

$$\hat{\rho}^{(0)} \xrightarrow{E^{(1)}(t)} \hat{\rho}^{(1)}(t), \quad \hat{\rho}^{(1)}(t) \xrightarrow{E^{(2)}(t)} \hat{\rho}^{(2)}(t), \quad \hat{\rho}^{(2)}(t) \xrightarrow{E^{(3)}(t)} \hat{\rho}^{(3)}(t), \quad \ldots, \quad \hat{\rho}^{(n-1)}(t) \xrightarrow{E^{(n)}(t)} \hat{\rho}^{(n)}(t) \tag{6}$$

where $\hat{\rho}^{(n)}$ is the nth order density matrix operator or the change in the density matrix due to the interaction with n electric fields and $E^{(n)}(t)$ is the nth applied electric field. We assume that the applied electric fields for well-separated pulses take the general form

$$E^{(n)}(\boldsymbol{r}, t) = \tilde{E}^{(n)}(t)e^{-i(\omega t - \boldsymbol{k}_n \cdot \boldsymbol{r})} + \tilde{E}^{(n)*}(t)e^{i(\omega t - \boldsymbol{k}_n \cdot \boldsymbol{r})} \tag{7}$$

where $\boldsymbol{r}$ is the coordinate of the molecule in the sample, $\boldsymbol{k}_n$ is the wave vector and must be different for all pulses, the product $\boldsymbol{k}_n \cdot \boldsymbol{r}$ includes any phase of the field, ω is the frequency of the electric field and is equal for all pulses, and $\tilde{E}^{(n)}(t)$ is the temporal shape of the pulse.

The FWM signal arises from molecules that have interacted with all three fields; therefore, in order to calculate the signal we need to obtain the third-order density matrix (see eqns. (1) and (2)). The detailed expressions of the density matrix in first-, second-, and third-order perturbation for a two-level system are shown in Appendix A. After the interaction with three consecutive pulses, the density matrix can be expressed as the contribution of two terms, each one with a different spatial dependency, $\boldsymbol{k}_{\text{VEcho}} = \boldsymbol{k}_1 - \boldsymbol{k}_2 + \boldsymbol{k}_3$ and $\boldsymbol{k}_{\text{Echo}} = -\boldsymbol{k}_1 + \boldsymbol{k}_2 + \boldsymbol{k}_3$. These components yield a polarization in each direction

$$P^{(3)}_{\text{VEcho}}(t) \propto \mu a_{21} b_{12} c_{21} \sin(\Omega_{21}(t - \tau) - (\boldsymbol{k}_3 - \boldsymbol{k}_2 + \boldsymbol{k}_1) \cdot \boldsymbol{r} \quad \text{and} \tag{8a}$$

$$P^{(3)}_{\text{Echo}}(t) \propto \mu a_{21} b_{12} c_{21} \sin(\Omega_{21}(t - \tau - 2\tau_{ab}) - (\boldsymbol{k}_3 + \boldsymbol{k}_2 - \boldsymbol{k}_1) \cdot \boldsymbol{r}). \tag{8b}$$

Here we assume that $\mu = \mu_{12} = \mu_{21}$. Note that the expression $\mu a_{21} b_{12} c_{21}$ yields μ^4 (see Appendix A). Therefore, the signal, which is proportional to the square of $P^{(3)}_{\text{VEcho}}(t)$, contains a factor of the dipole moment, μ, to the eighth power. This is in agreement with the expression for the susceptibility (eqn. (3)). The control mechanism is apparent in the expression of $\hat{\rho}^{(2)}(t)$

$$P^{(2)}_{11} = 2\left(\frac{i}{\hbar}\right)^2 a_{21} b_{12} \cos(\Omega_{21}\tau_{ab} - (\boldsymbol{k}_1 - \boldsymbol{k}_2) \cdot \boldsymbol{r}) \quad \text{and} \tag{9a}$$

$$P^{(2)}_{22} = -2\left(\frac{i}{\hbar}\right)^2 a_{21} b_{12} \cos(\Omega_{21}\tau_{ab} - (\boldsymbol{k}_1 - \boldsymbol{k}_2) \cdot \boldsymbol{r}) \tag{9b}$$

where the control parameter is the time delay τ_{ab} between the first two pulses. In the particular case of a two-level system, τ_{ab} can be used to turn on and off the population transfer into the ground and excited states. Because only one transition frequency is involved, in this case $|\Omega_{21}|$, the perturbative solution indicates that τ_{ab} can only be used to control the values for $\rho^{(2)}_{11}$ and $\rho^{(2)}_{22}$ simultaneously. For a three-pulse FWM experiment with more than one transition frequency, τ_{ab} can be used to control the population transfer between the ground and excited states. This situation is considered next using a four-level system. The issue of coherent control over Liouville space has been addressed by Wiersma's group for a heterodyne detected signal where virtual echo and echo signals coincide in space.[17]

2.4. Four-level system

For the four-level system, we will include two electronic states with two vibrational levels each, we will denote them as $|1\rangle$, $|2\rangle$, $|3\rangle$ and $|4\rangle$. As the three electric fields interact with the system, the density matrix evolves as

$$\begin{pmatrix} \rho_{11}^{0} & 0 & 0 & 0 \\ 0 & \rho_{22}^{0} & 0 & 0 \\ 0 & 0 & 0 & 0 \\ 0 & 0 & 0 & 0 \end{pmatrix} \xrightarrow{E^{(1)}(t)} \begin{pmatrix} 0 & 0 & \rho_{31}^{(1)*} & \rho_{41}^{(1)*} \\ 0 & 0 & \rho_{32}^{(1)*} & \rho_{42}^{(1)*} \\ \rho_{31}^{(1)} & \rho_{32}^{(1)} & 0 & 0 \\ \rho_{41}^{(1)} & \rho_{42}^{(1)} & 0 & 0 \end{pmatrix} \xrightarrow{E^{(2)}(t)}$$

$$\begin{pmatrix} \rho_{11}^{(2)} & \rho_{21}^{(2)*} & 0 & 0 \\ \rho_{21}^{(2)} & \rho_{22}^{(2)} & 0 & 0 \\ 0 & 0 & \rho_{33}^{(2)} & \rho_{43}^{(2)*} \\ 0 & 0 & \rho_{43}^{(2)} & \rho_{44}^{(2)} \end{pmatrix} \xrightarrow{E^{(3)}(t)} \begin{pmatrix} 0 & 0 & \rho_{31}^{(3)*} & \rho_{41}^{(3)*} \\ 0 & 0 & \rho_{32}^{(3)*} & \rho_{42}^{(3)*} \\ \rho_{31}^{(3)} & \rho_{32}^{(3)} & 0 & 0 \\ \rho_{41}^{(3)} & \rho_{42}^{(3)} & 0 & 0 \end{pmatrix} \tag{10}$$

Again, following the first pulse, we recover only matrix elements of the form $\rho_{ge}^{(1)}(t)$ (upper right block) and $\rho_{eg}^{(1)}(t)$ (lower left block) as shown in the first step of eqn. (10). As noted earlier, after the interaction with two electric fields, the change of the density matrix represents the populations transferred to the ground and excited states; the $\rho_{gg}^{(2)}$ terms (upper left) and $\rho_{ee}^{(2)}$ terms (lower right) and the time-dependent vibrational coherence in each electronic state, $\rho_{gg}^{(2)}(t)$ and $\rho_{ee}^{(2)}(t)$ are non-zero for $\rho^{(2)}(t)$. In order to calculate the signal we need to obtain $\hat{\rho}^{(3)}(t)$ (see eqn. (1) and eqn. (2)). The detailed expression for the density matrix in the first-, second-, and third-order interaction for a four-level system are shown in Appendix B. As can be seen from the equations in Appendix B, each matrix element $\rho_{ge}^{(3)}(t)$ can be separated into one contribution which depends only on the dynamics of the ground state and another contribution which depends only on the dynamics of the excited state. Since the polarization is a linear function of $\hat{\rho}^{(3)}(t)$ (see eqn. (2)), these two contributions persist in the expression of $P^{(3)}(t)$; therefore, the signal becomes

$$I_{\mathrm{FWM}}(\tau_{\mathrm{ab}}, \tau) \propto \mu^2\alpha^6\left[\int (P_{\mathrm{g}}^2(t) + P_{\mathrm{e}}^2(t) + 2P_{\mathrm{e}}P_{\mathrm{g}}(t))\,\mathrm{d}t\right]. \tag{11}$$

Notice that $\mu^2\alpha^6$ gives μ to the eighth power, agreeing with the earlier formulation in the two-level system and with the expression of the susceptibility in eqn. (3). The first part of eqn. (11) corresponds to ground state motion (S_{gg}), the second term represents excited state motion (S_{ee}), and the last term corresponds to the cross terms (S_{ge}) containing various frequencies which average to a small overall amplitude and hence is a minor contribution to the signal. After integration of eqn. (11), we obtain

$$I_{\mathrm{FWM}}(\tau_{\mathrm{ab}}, \tau) \propto \mu^2\alpha^6(S_{\mathrm{gg}}(\tau_{\mathrm{ab}}, \tau) + S_{\mathrm{ee}}(\tau_{\mathrm{ab}}, \tau) + S_{\mathrm{ge}}(\tau_{\mathrm{ab}}, \tau)) \tag{12}$$

where the two main terms for PS-I are

$$S_{\mathrm{gg}}^{\mathrm{I}}(\tau_{\mathrm{ab}}, \tau) = [(1 + w^2) + (1 + \omega^2)\cos(\omega_{\mathrm{e}}\tau_{\mathrm{ab}})](1 + \cos(\omega_{\mathrm{g}}\tau)) \qquad \text{and} \tag{13}$$

$$S_{\mathrm{ee}}^{\mathrm{I}}(\tau_{\mathrm{ab}}, \tau) = [(1 + w^2) + (1 - w^2)\cos(\omega_{\mathrm{g}}\tau_{\mathrm{ab}})](1 + \cos(\omega_{\mathrm{e}}\tau)) \tag{14}$$

where $w = \rho_{11}^{(0)} - \rho_{22}^{(0)}$. Therefore, S_{gg} depends on $\cos(\omega_{\mathrm{g}}\tau)$ and is a modulating signal with vibration period τ_{g} (with $\tau_{\mathrm{g}} = 2\pi/\omega_{\mathrm{g}}$) in the ground state; S_{ee} depends on $\cos(\omega_{\mathrm{e}}\tau)$ and is a modulating signal with vibration period τ_{e} (with $\tau_{\mathrm{e}} = 2\pi/\omega_{\mathrm{e}}$) in the excited state.

The amplitude of the modulation depends on the delay between the first two pulses ($\tau_{\mathrm{ab}} = t_2 - t_1$). For the S_{gg} component, this amplitude depends on $\omega_{\mathrm{e}}\tau_{\mathrm{ab}}$, and for the S_{ee} component, this amplitude depends on $\omega_{\mathrm{g}}\tau_{\mathrm{ab}}$. This effect already appears in a second-order density matrix after the interaction with the two pulses as seen in

$$\tilde{\rho}_{\mathrm{gg}}^{(2)}(t_3) - \tilde{\rho}_{\mathrm{g'g}}^{(2)}(t_3) \propto \cos\left(\frac{\omega_{\mathrm{e}}\tau_{\mathrm{ab}}}{2}\right)\cos\left(\frac{\omega_{\mathrm{g}}\tau}{2}\right) \qquad \text{and} \tag{15}$$

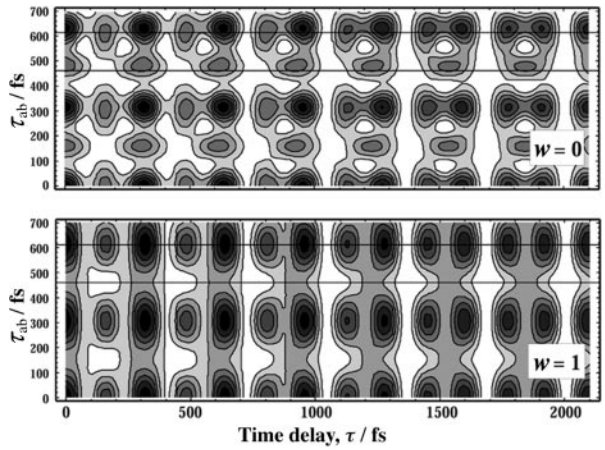

Fig. 4 Simulated I_2 dynamics for **PS-I** according to eqns. (13) and (14). Signal intensity is plotted as a function of fixed time delay τ_{ab} between fields E_a and E_b along the *y*-axis and as a function of variable time delay τ between fields E_b and E_c along the *x*-axis. Darker areas correspond to more intense signal. The simulations are shown for two extreme values of the population parameter, $w = 0$ (top) and $w = 1$ (bottom). The thin horizontal lines at $\tau_{ab} = 614$ fs and 460 fs correspond to the values of τ_{ab} used for the experimental data shown in Figs. 5–9.

$$\tilde{\rho}^{(2)}_{ee}(t_3) + \tilde{\rho}^{(2)}_{ee}(t_3) \propto \left[\cos\left(\frac{\omega_g \tau_{ab}}{2}\right) - iw \sin\left(\frac{\omega_g \tau_{ab}}{2}\right)\right]\cos\left(\frac{\omega_e \tau}{2}\right). \quad (16)$$

If $\cos(\frac{1}{2}\omega_e \tau_{ab}) = 0$, the signal from the ground state vibration disappears (eqn. (15)) and we will see pure excited state dynamics. This effect occurs for $\tau_{ab} = \tau_e\ (n + \frac{1}{2})$. In the general case for the excited state component where w is not specified, it is not possible to eliminate this term by a choice of τ_{ab} because of the cosine and sine components (eqn. (16)). Therefore, at least one term will always be significant. However, this component can be eliminated when $w = 0$ (*i.e.*, equal excitation from the two lower levels) by setting $\tau_{ab} = \tau_g\ (n + \frac{1}{2})$. For $w \neq 0$, we cannot attain complete control of the excited state but for many values of τ_{ab}, it becomes less dominant.

Using eqns. (12)–(14), we can simulate the dynamics that should be obtained for **PS-I** experimental data as the values for τ_{ab} and τ are varied. This simulation is shown as a contour plot in Fig. 4 with τ along the *x*-axis and τ_{ab} along the *y*-axis. For $w = 0$ and $\tau_{ab} = (n + \frac{1}{2})\tau_e$ (155 and 465 fs), we see only excited state dynamics with a vibrational period of 307 fs; for $w = 0$ and $\tau_{ab} = n\tau_e$ (310 and 620 fs), we obtain both ground and excited state dynamics with an apparent vibrational period of 160 fs. Pure ground state should be observed at $\tau_{ab} = (n + \frac{1}{2})\tau_g$ (80, 240, 400 and 560 fs) when $w = 0$. If $w = 1$ and $\tau_{ab} = (n + \frac{1}{2})\tau_e$, we can see only excited state dynamics. If $w = 1$ and $\tau_{ab} = n\tau_e$, we again see ground and excited state dynamics.

3. Experimental

The experimental set-up has been described previously.[12] These experiments were carried out with 65 fs (FWHM) pulses centered at 620 nm generated by a CPM femtosecond laser system. After amplication by a four-stage dye amplifier pumped by a 30 Hz Nd-YAG laser, the pulses had an average pulse energy of 0.35 mJ. To avoid saturation of transitions and high intensity effects, the laser was attenuated. The pulses were characterized using a frequency-resolved optical gating (FROG) instrument to determine the chirp.

The laser was split into three non-phase-locked beams of comparable intensity (see Fig. 1), which were combined at the sample by a 0.5 m focal length lens in the forward box geometry[18,19] with one inch sides. Field E_c could be scanned in time by a computer-controlled actuator. Field E_b was on a manual translator and could be advanced or delayed in time with respect to field E_a. When separating pulses E_a and E_b by $\tau_{ab} = (n + \frac{1}{2})\tau_e$, we advanced the translator by 460 fs ($n = 1$) rather than 153 fs ($n = 0$) to avoid a possible temporal overlap of the laser pulses. Similarly, we

used 614 fs rather than 307 fs for $\tau_{ab} = n\tau_e$ measurements. The homodyne signal was collected in the $\boldsymbol{k}_s = \boldsymbol{k}_a - \boldsymbol{k}_b + \boldsymbol{k}_c$ phase-matched direction (see Fig. 1). The signal was collected with a spectrometer set at the central wavelength of the laser pulse, typically 620 nm. Unless otherwise noted, the spectrometer was used at low spectral resolution ($\approx$8–16 nm FWHM) to avoid spectral filtering.

The experiments were performed on neat iodine vapor in a static quartz cell at 140 °C (160 Torr). Transients were obtained by scanning the time delay between E_c (the variable beam) and E_a and E_b (the fixed beams); these transients reveal the time evolution of the molecular dynamics in I_2. Typically, the signal was collected at each time delay for 10 laser shots, discarding any data points corresponding to pulses with energy more than one standard deviation from the mean. Most transients were taken for 200 different time delays and averaged for 20 scans.

4. Results and discussion

4.1. Pulse sequence I: Ground and excited state dynamics

The data shown in Fig. 5 correspond to a transient grating measurement with fields E_a and E_b overlapped in time ($\tau_{ab} = 0$) for PS-I. The long undulation ($\approx$1.5 ps) corresponds to the early dephasing in the rotational anisotropy. The fast oscillation corresponds to ground and excited state vibrations, which are excited impulsively by the short pulse lasers. The Fourier transform of the transient (only the first 5 ps of the data are shown) clearly shows a peak at 110 cm^{-1} that corresponds to the excited state vibrational frequency. A peak at 210 cm^{-1}, corresponding to the ground state dynamics, is also observed with similar amplitude. This type of data has been analyzed previously in an earlier publication from our group.[12] Other groups have also observed similar results when carrying out FWM measurements on molecular iodine.[20–22]

Based on the spectrum of our pulses, the sample temperature, and the Franck–Condon factors, we can determine which states contribute to the ground and excited state dynamics. For the ground state, the observed motion arises from a linear superposition of states $v'' = 2$–4 with a collective frequency of 160 fs. Although levels $v'' = 0$ and 1 are the ones which are most populated in the sample at 140 °C before the interaction with the laser pulses, the Franck–Condon overlap between these levels and the excited state at 620 nm is very small.[23] For the excited state, the observed motion arises from a linear superposition of states $v' = 6$–11 in the B state, with a collective frequency of 307 fs.[24,25]

When field E_a acts on the sample before field E_b, the sample has a certain amount of time (τ_{ab}) to evolve. We have explored how to use the time dependence of the molecular system for controlling the excitation process. Fig. 6 shows the three pulse FWM transient for PS-I with τ_{ab} equal to 614 fs ($2\tau_e$). We choose $2n\tau_e$ rather than $(n + \frac{1}{2})\tau_g$ in order to have the maximum ground state

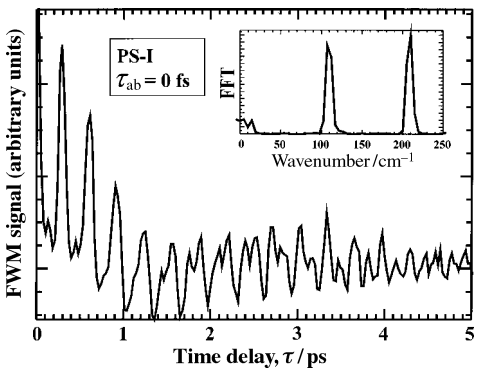

Fig. 5 Experimental transient for PS-I where $\tau_{ab} = 0$ fs and thus fields E_a and E_b are overlapped in time. Only the first 5 ps of the data are shown. The insert shows the power FFT of the time data and reveals frequencies of 110 cm^{-1} and 210 cm^{-1} corresponding to the excited and ground state vibrations of molecular iodine, respectively.

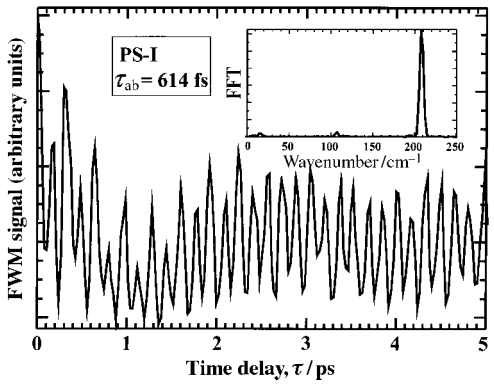

Fig. 6 Experimental transient for PS-I where τ_{ab} = 614 fs (only the first 5 ps are shown). This value of τ_{ab} is equivalent to two vibrational periods of the excited state of iodine ($2\tau_e$). Observed vibrations have a period of 160 fs. The power FFT of the transient shows a predominant frequency of 208 cm^{-1} corresponding to vibrations of the ground $X\,^1\Sigma_{o+g}$ state of molecular iodine. It depicts that the detected FWM signal is predominantly from the ground state. There is a minor peak at 107 cm^{-1} corresponding to a small contribution from the excited state. Note that the slow dip in modulation around 1.5 ps is due to rotational dephasing.

contribution (see Fig. 4). From the transient, we observe a series of fast oscillations with a period of 160 fs, and a slow undulation with a dip at 1.5 ps. The Fourier transform of this transient (only the first 5 ps are shown) shows a dominant peak at 208 cm^{-1}, the vibrational frequency of the ground state, and a small peak at 16 cm^{-1}, corresponding to the rotational dephasing. The observed dynamics correspond almost exclusively to the ground $X\,^1\Sigma_{o+g}$ state.[26] A small peak at 107 cm^{-1} is also observed indicating a small contribution from the excited state as expected from the theory section.

When τ_{ab} in PS-I is set equal to 460 fs, corresponding to one and a half vibrational periods of the excited state ($3/2\ \tau_e$), a large change in the three-pulse FWM transient is observed. Fig. 7 shows a long undulation that dips around 1 ps and a fast oscillation with a period of 307 fs. The Fourier transform of the data (only the first 5 ps are shown) shows a dominant peak at 108 cm^{-1} corresponding to vibrations in the excited state. A small peak at low frequencies caused by rotational dephasing can also be seen. A small contribution at 218 cm^{-1} is also observed but it can be

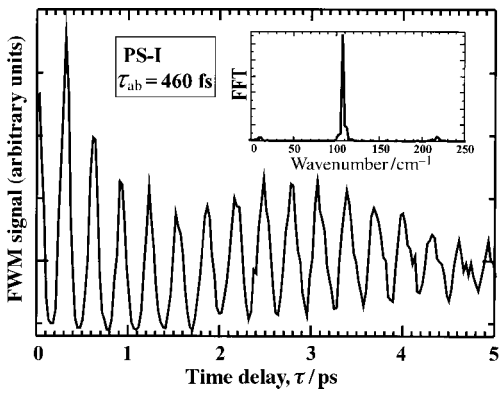

Fig. 7 Experimental transient for PS-I (only the first 5 ps are shown) where τ_{ab} = 460 fs corresponding to one and a half vibrational periods of iodine in the excited state ($3/2\tau_e$). Observed vibrations have a period of about 307 fs. The power FFT of the transient shows a predominant frequency of 108 cm^{-1} corresponding to vibrations of the excited $B\,^3\Pi_{o,u}$ state of molecular iodine. It reflects that the detected FWM signal detected is exclusively from the excited state. The slow modulation with a dip near 1 ps is due to rotational dephasing.

assigned to the second harmonic of the excited state oscillation. In this case, the dynamics are consistent with the excited $\mathbf{B}\,^3\Pi_{o,u}$ state.[24,25]

In Fig. 8 we show a close up of the three-pulse FWM transients shown in Figs. 6 and 7. Both of these transients were taken under identical conditions, one immediately following the other, making sure that the only parameter that changed was the delay τ_{ab}. It is clear that for early times, every second oscillation in the $\tau_{ab} = 614$ fs data coincides with an oscillation in the $\tau_{ab} =$ 460 fs data; however, at longer times, a clear mismatch is observed in this pattern. The mismatch is caused by the difference in spectroscopic parameters of the ground and excited states of iodine. This implies that the observed dynamics in the $\tau_{ab} = 614$ fs case are not caused by a doubling of the observed excited state frequency. Therefore τ_{ab} can be used to control what dynamics are observed. In the theory section, we calculated what values are required to observe maximum control. For all $\tau_{ab} = (n + \frac{1}{2})\tau_e$, excited state dynamics are expected; for $\tau_{ab} = (n + \frac{1}{2})\tau_g$, ground state dynamics are expected. Fig. 4 shows that there is a wide range of values where the observed result is quite similar. Also evident in Fig. 4 is the mismatch between the excited state beat and every other ground state beat as time evolves.

In Fig. 9 we examine the difference in the Fourier transforms for $\tau_{ab} = 460$ fs and 614 fs as shown in Figs. 6 and 7. We first highlight the selectivity of this method for detecting ground or excited state dynamics. For $\tau_{ab} = 460$ fs, we observe a dominant peak at 108 cm^{-1} corresponding to the excited state; a small peak at 218 cm^{-1} is most certainly due to the second harmonic of the same dynamics given that the FFT shows no amplitude at 208 cm^{-1}. For $\tau_{ab} = 614$ fs, we observe a peak at 208 cm^{-1} that corresponds to the ground state vibrational frequency. For this time delay between fields E_a and E_b, we also see a minor peak at 107 cm^{-1} that indicates a small contribution from the excited state. The insert shows the low frequency end of the Fourier transform with two distinguishable contributions. The moment of inertia of the X state is quite different from that of the B state; the rotational constants are 0.03696 and 0.02764 cm^{-1}, respectively.[25,26] This difference is manifested in the low frequency components due to the differences in the rotational dephasing dynamics. The observed positions are 11 ± 1 and 16 ± 1 cm^{-1}, respectively. The ratio between these positions is 1.5 ± 0.3 and the ratio of the rotational constants is 1.34; these are in fair agreement. This observation is further proof that the dynamics correspond primarily to the ground or the excited state. Based on Figs. 8 and 9, we confirm that the time delay τ_{ab} can be used to control the transfer of population between the ground and excited states.

We have used three-pulse FWM to measure the vibrational coherence dephasing time of the ground or excited state by using τ_{ab} to control their relative contribution. The results of these measurements give additional support to the control between the populations. These results, as a function of temperature and buffer gases, will be published elsewhere.[27]

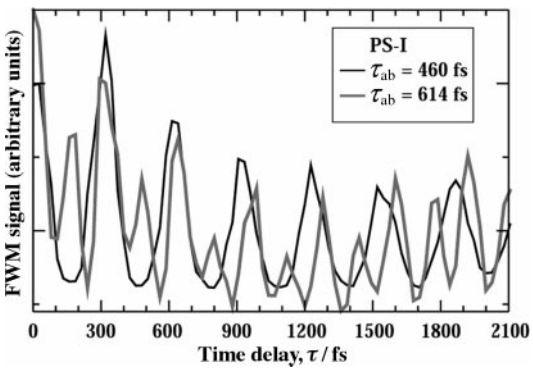

Fig. 8 Close-up of the time data shown in Figs. 6 and 7. Notice that the two transients are in-phase at early times and are out-of-phase after the first picosecond. The dephasing of the two data sets supports the fact that they originate from two different states of molecular iodine. In other words, one is not the second harmonic of the other. The thin dark line shows the vibrations in the excited state with $\tau_{ab} = 460$ fs, while the thick gray line shows the vibrations of the ground state with $\tau_{ab} = 614$ fs.

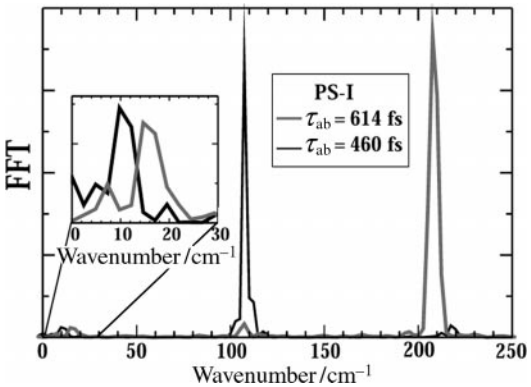

Fig. 9 Close-up of the power FFT for the transients shown in Figs. 6 and 7. When $\tau_{ab} = 614$ fs (gray line), the data show a small contribution at 107 cm^{-1} and a prominent peak at 208 cm^{-1}, corresponding to the vibrational frequency of the ground state. When $\tau_{ab} = 460$ fs (black line), the data show a prominent peak at 108 cm^{-1}, corresponding to the vibrational frequency of the excited state, and a minor peak at 218 cm^{-1}, which is most likely a second harmonic of the 108 cm^{-1} peak. The insert shows the enlarged region at low frequencies with peaks at 16 ± 1 and 11 ± 1 cm^{-1}. These correspond to the different rotational dephasing dynamics occurring in the **X** state ($\tau_{ab} = 614$ fs) and the **B** state ($\tau_{ab} = 460$ fs), respectively. The difference in the frequency is caused by the difference in the moment of inertia between these two states. These data confirm the ability to select ground or excited state dynamics based on the choice of τ_{ab} in three-pulse FWM.

4.2. Pulse sequence II: Coherence dynamics

The previous data in Figs. 5–9 show how the delay between the first two pulses in PS-I can be used to control which type of dynamics are observed, ground or excited state. It is interesting to ask what are the relevant dynamics of the system after a single interaction with the electric field that influence the control process. In Section 2 we theoretically discussed the coherence $\rho_{eg}^{(1)}$ formed between ground and excited states after a single interaction with the electric field E_a. One can carry out an experimental observation of these dynamics by having field E_c interact with the system and, after a variable time delay τ, have fields E_b and E_a interrogate the system (PS-II). Note that in our experiments, fields E_a and E_c are interchangeable; for practical reasons we have carried out measurements with beam E_c preceding beams E_b and E_a. Such an experimental set-up, also known as a reverse-transient grating,[12,28] yielded the data in Fig. 10 (only the first 5 ps are shown) with $\tau_{ab} = 0$ (E_b and E_a overlapped). As before, the slow picosecond undulation is due to rotational dephasing dynamics the vibrations are due to ground and excited state frequencies as seen in

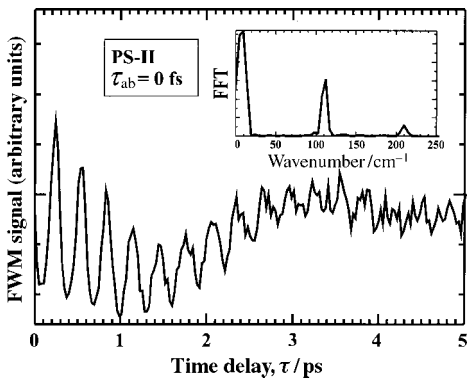

Fig. 10 Experimental transient for PS-II where $\tau_{ab} = 0$ fs and thus fields E_b and E_a are overlapped in time. Only the first 5 ps of the data are shown. The insert shows the power FFT of the time data. The FFT reveals frequencies of 110 cm^{-1} and 210 cm^{-1} corresponding to the excited and ground state vibrations of molecular iodine, respectively. The intensity of the ground state peak is much smaller than the one corresponding to the excited state.

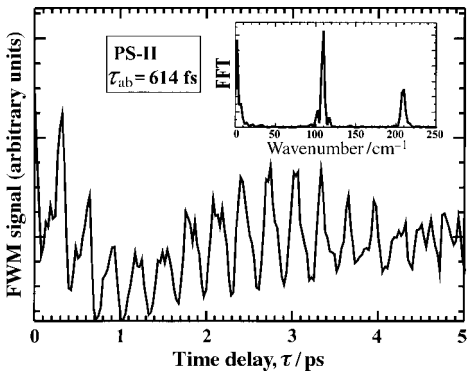

Fig. 11 Experimental transient for PS-II where $\tau_{ab} = 614$ fs (only the first 5 ps are shown). The power FFT of this transient shows frequencies at both 108 cm^{-1} and 208 cm^{-1}. Note that for this value of τ_{ab}, there is an increase in the amount of ground state contribution as compared to the case $\tau_{ab} = 0$ (see Fig. 10).

the Fourier transform. Notice that during the first picosecond, the 307 fs oscillations that correspond to the vibrational frequency of the excited state dominate the transient.

In the theory section, we discussed the signal dependence on τ_{ab} and τ for PS-I. Converting the formalism to PS-II turns out to be quite simple. For this, we will maintain the definition of τ_{ab} as a fixed time delay and τ as the time that is scanned. Note that for PS-II, τ is the delay between the first two pulses (t_2-t_1) and τ_{ab} is the delay between the last two pulses (t_3-t_2). The expression for the ground and excited state contributions to the signal, eqns. (13) and (14), need to be modified accordingly by interchanging τ_{ab} and τ. Notice that this modification converts the ground (excited) to an excited (ground) state contribution. The resulting equations are

$$S^{II}_{gg}(\tau_{ab}, \tau) = [(1 + w^2) + (1 + w^2)\cos(\omega_g \tau)](1 + \cos(\omega_e \tau_{ab})). \quad (17)$$

$$S^{II}_{ee}(\tau_{ab}, \tau) = [(1 + w^2) + (1 + \omega^2)\cos(\omega_e \tau)](1 + \cos(\omega_g \tau_{ab})) \quad (18)$$

Based on these expressions, one can use the fixed delay τ_{ab} to 'filter' the ground and excited state dynamics.

In Figs. 11 and 12 we have explored the possibility of using the delay time τ_{ab} between beams E_b and E_a to filter the type of dynamics that are observed. The data in Fig. 11 (only the first 5 ps are shown), which was taken with $\tau_{ab} = 614$ fs, show an increase in the amount of ground state

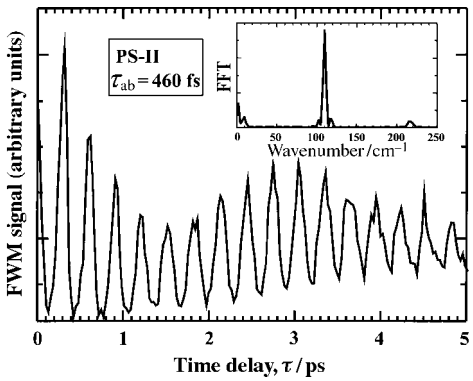

Fig. 12 Experimental transient for PS-II where $\tau_{ab} = 460$ fs (only the first 5 ps are shown). Notice the well-resolved oscillations with a period of 307 fs. The power FFT of this transient shows a predominant frequency of 108 cm^{-1} corresponding to vibrations of the excited state. A minor contribution at 218 cm^{-1} is most probably a second harmonic of the 108 cm^{-1} component.

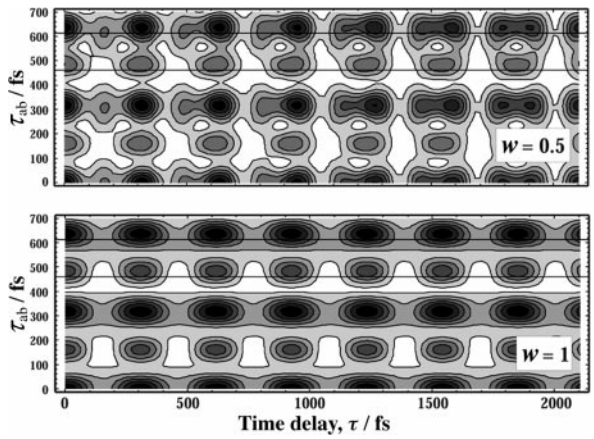

Fig. 13 Simulated I_2 dynamics for PS-II according to eqns. (17) and (18). Signal intensity is plotted as a function of fixed time delay τ_{ab} between fields E_b and E_a along the y-axis and as a function of variable time delay τ between fields E_c and E_b along the x-axis. The darker areas correspond to more intense signal. Simulations are shown for two values of the initial population parameter, $w = 0.5$ (top) and $w = 1$ (bottom). The thin horizontal lines at τ_{ab} of 614 fs and 460 fs correspond to the experimental data shown in Figs. 10–12 and reflect excellent agreement between experiment and theory (see text).

contribution as compared to the contribution when $\tau_{ab} = 0$ fs. This difference is evident by comparing the 210 cm^{-1} peaks in the Fourier transforms in Figs. 10 and 11. The data in Fig. 12 (only the first 5 ps are shown), which was taken with $\tau_{ab} = 460$ fs, show excited state dynamics. The small contribution at 218 cm^{-1} is due to the second harmonic of the excited state dynamics. These experiments show that the delay τ_{ab} between fields E_b and E_a can be used effectively to filter the relative contributions from ground or excited state dynamics in the initially prepared coherence. We note that this filter does not provide the same amount of control as can be achieved with PS-I.

We estimate that the ground vibrational states which have the most important contributions are $v'' = 3$ and 4, with that from $v'' = 3$ being approximately twice that of $v'' = 4$. This is based on a calculation using the Boltzmann distribution of the initial states, the spectroscopic parameters of both states, the Franck–Condon factors, and the spectrum of the laser. Therefore, $w = 0.5$ is a good estimate to use in our simulations for the initial population distribution. Using eqns. (17) and (18), we obtain Fig. 13 showing the possible dynamics that can be observed for PS-II. We can see that for $w = 0.5$ and $\tau_{ab} = 460$ fs, we should obtain only excited state dynamics; for $w = 0.5$ and $\tau_{ab} = 614$ fs, we should see ground state dynamics with every other peak being much weaker. These simulations confirm our experimental observations and show that we cannot obtain the same degree of control as was possible for PS-I. If $w = 1$, we would only see excited state dynamics with either value of τ_{ab}. Therefore $w = 1$ is not a good assumption for our measurements and this comparison indicates that $w = 0.5$ is a much better approximation. Of course, to simulate the experiment more accurately, more levels in both the ground and the excited states are required.

4.3. Time-resolved and spectrally dispersed three-pulse FWM measurements

The signal from all experiments presented here arises from a third-order polarization of the system, $P^{(3)}(t)$, see Section 2. The decay of the polarization is determined by the coherence between the ground and the excited states, a T_2 process. For iodine at the experimental temperature (140 °C), the dephasing time is >100 ps.[27] Because the emission time is long compared to the femtosecond dynamics of the system, the signal carries with it spectroscopic information about the transition. Based on the theory, emission from $P^{(3)}(t)$ involves frequencies from each of the vibrational levels of the excited state that are coherently excited by the first laser interaction. Fig. 14 shows a spectrum of the signal (black line) and a spectrum of the laser (gray line). The signal spectrum was taken with a three-pulse FWM PS-I experiment where the delay between fields E_a and E_b was 460 fs and field E_c arrived 1.2 ps after field E_b. It is clear that the signal is not a replica

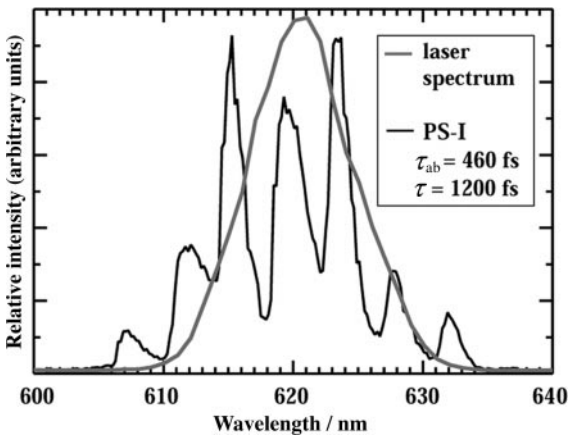

Fig. 14 Spectrum of the laser used for the experiments (thick gray line) and spectrum of three-pulse FWM signal detected for **PS-I** with $\tau_{ab} = 460$ fs and $\tau = 1200$ fs showing well-defined transitions. The intensities of the individual peaks are found to vary as a function of τ (not shown). The FWHM of the peaks is approximately 2 nm. The peak maxima have a spacing of approximately 110 cm^{-1} (4 nm) reflecting the frequency difference between the vibrational levels in the excited state.

of the laser. The well-defined transitions have a spacing of 110 cm^{-1} (4 nm) that corresponds to the frequency difference between vibrational levels in the excited state, as expected. The spectrum shown was taken with a resolution corresponding to $\approx$2 nm (250 μm slits). Further reduction of the spectrometer slits (down to 120 μm, equivalent to 1 nm) did not show higher spectral resolution.

Based on a dephasing time of 100 ps, one would expect a bandwidth of 0.053 cm^{-1}. The observed width of the spectral transition (FWHM $\approx$ 2 nm) observed corresponds to 52 cm^{-1}. One must remember that the experiment is carried out at 140 °C; therefore, a very large rotational broadening is expected. We estimate this broadening to be of the order of 20 cm^{-1}. The additional broadening is due to a near coincidence of spectroscopic transitions. For example, $v' = 9$ to $v'' = 3$ occurs at 619.2 nm and $v' = 11$ to $v'' = 4$ occurs at 618.8 nm. The seven spectral features in the spectrum can be tentatively assigned to three different progressions: transitions from levels $v' = 8$–14 to $v'' = 4$; from $v' = 6$–12 to $v'' = 3$, and $v' = 4$–10 to $v'' = 2$. The most intense transitions involve $v'' = 3$.

The spectrum of Fig. 14 shows that the signal contains enough spectral resolution that we can follow the time-resolved dynamics at each wavelength and obtain a better understanding of the system. We can follow the dynamics of the population formed after the first two pulses by plotting the observed signal as a function of time τ and wavelength. We have carried out such measurements with $\tau_{ab} = 460$ and 614 fs. They will be published elsewhere.[11] The most important point is that for all cases we reproduce the observed control. For both values of τ_{ab}, we see deviations in the phase at the most extreme wavelengths (605 and 632 nm). These deviations are a manifestation of the fact that one requires a model with more levels to simulate this system properly where all the contributing states with their inherent anharmonicity are included.

4.4. The effect of pulse chirp on three-pulse FWM measurements

So far we have used three-pulse FWM to follow the vibrational dynamics of molecules in the ground and excited states. We now turn our attention to observing the effect that linear chirp has on this type of experiment. In Fig. 15 we present three transients obtained for positive (2500 fs^2), zero, and negative (-2500 fs^2) linear chirps. For these measurements we used **PS-I** and kept fields E_a and E_b overlapped in time. The data show ground and excited state dynamics as expected for an experiment with $\tau_{ab} = 0$. Note that the time resolution of the experiments is not affected by the magnitude of the chirp. The pulses for these measurements were 65 fs when the chirp was zero and 120 fs for the maximum positive and negative chirps. The time resolution in these experiments is determined by the spectral bandwidth of the laser pulses.[10,29]

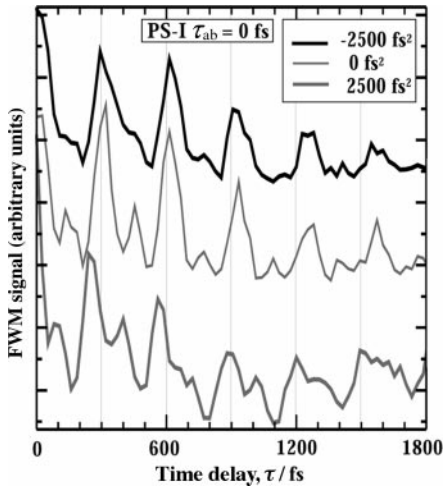

Fig. 15 Experimental three-pulse FWM signals detected for PS-I with $\tau_{ab} = 0$ fs and laser pulses chirped to -2500 fs^2 (top—thick dark line) and $+2500$ fs^2 (bottom—thick gray line). For comparison, the signal detected when the pulses were transform-limited (chirp of 0 fs^2) is also shown (middle—thin line). A change in the amount of ground state contribution is observed in all three cases. Also a change in the period of vibration is evident for the positively chirped case.

As seen in Fig. 15, the difference between the zero and negative chirp data is an apparent reduction in the amplitude of the observed ground state oscillations for negative chirp. The data obtained with positive chirp shows more amplitude in the ground state vibrations and the oscillations seem to be phase shifted by about 70 fs. These differences are caused by the chirped fields launching the different components of the coherent wave packet with phase shifts. The effect of chirp on wave packet dynamics on iodine has been studied extensively by various groups.[30–35] We are working on a multi-level model that takes into account chirp in the electric field to simulate our data.[36]

Fig. 16 contains the spectrally dispersed spectra resulting for three-pulse FWM measurements carried out with $\tau_{ab} = 460$ fs and the time delay $\tau = 600$ fs in PS-I. All the spectra shown were taken under identical conditions; they have not been scaled. The only variable in this data set was

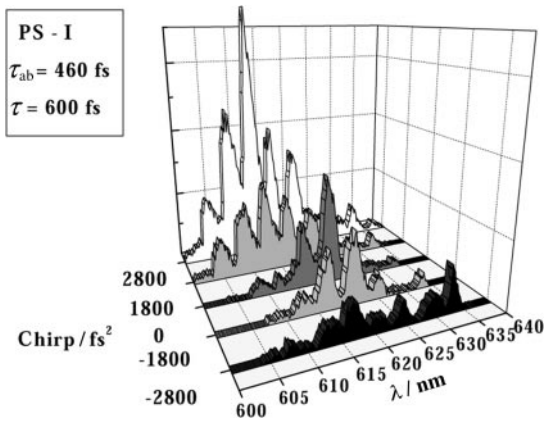

Fig. 16 Spectrally dispersed three-pulse FWM data obtained for PS-I with $\tau_{ab} = 460$ fs and $\tau = 600$ fs when differently chirped pulses were applied. It is clear that for chirps of $+2800$ fs^2, the predominant peaks are at shorter wavelengths and the main peak is at 615 nm. The center of the spectrum gradually shifts to longer wavelengths as the chirp values are swept from positive to negative values. At a chirp of -2800 fs^2, the most intense peak is centered about 632 nm.

the linear chirp of the laser pulses for each measurement. In Fig. 16 we see that positive chirps, red frequencies before blue, cause the higher energy components to be more intense while the low frequency components (633 nm) have less intensity. The situation is reversed for negatively chirped fields. These differences can be attributed to two different processes. First, different spectral components of the signal have slightly different dynamics and the chirp highlights the phase differences between them. Second, there may be preferential excitation of higher or lower vibrational states because of the chirp in the laser pulses. This effect may be related to adiabatic passage processes in stimulated emission, a process that has also been shown with chirped pulses.[37–40] The effect of chirp in three-pulse FWN is explored elsewhere.[11]

5. Conclusions

In this paper, we have demonstrated the usefulness of three-pulse FWM for studying and controlling processes that are initiated by laser excitation. We outlined the theory based on the density matrix formalism and solved it for two- and four-level systems. Expressions for the four-level system, based on PS-I, indicate that the populations in the ground and excited states can be controlled by the time delay between the first two electric field interactions. Experiments were found to be in excellent agreement with the theory. We introduced a second pulse sequence, PS-II, to observe the time evolution of ground or excited state components of the coherence induced by the first electric field. Experimental results showed that this technique works well for following excited state dynamics. Theoretical calculations support the observation and show that in some cases only excited state dynamics can be selected.

Three-pulse FWM, being a phase-matched technique, ensures that the signal arises only from those molecules that have interacted with the three fields. The technique as presented here is ideal for studying laser control because it uses the intramolecular dynamics time scale. Scherer *et al.* showed that phase-locked laser pulses could be used to enhance the excitation of molecular iodine when the pulses were combined in-phase.[41] Multiple-pulse techniques that lack a phase-matching condition or that are performed without phase-locked pulses can result in signal deriving from molecules that have interacted with only two of the laser pulses and not all three of them. In these cases, the signal can be simply simulated by a sum of two separate experiments and the 'control' feature is not demonstrated or observed.

Several experimental parameters were varied to explore the role of τ_{ab}, τ, collection wavelength and chirp in three-pulse FWM. The dispersed spectrum of the three-pulse FWM signal revealed well-defined spectroscopic transitions. Selective wavelength collection gives a third dimension to this technique that can be used to follow the amplitude of different quantum levels of the system as a function of τ_{ab} and τ.

Schmitt *et al.* studied molecular iodine with a time-resolved four-wave mixing technique in which the first two pulses were overlapped in time.[21] When they detected at frequencies higher than the carrier frequency of the laser, ground state dynamics were observed. For lower frequency detection, excited state dynamics were observed. They attributed this observation to spectral filtering of anti-Stokes and Stokes contributions to the signal, respectively. We have observed similar effects for $\tau_{ab} = 0$; however, we find that for three-phase FWM, the pulse sequence, in particular τ_{ab}, determines what types of dynamics are observed. This is because the pulse sequence can be used to eliminate the ground, or in some cases, the excited state contributions. PS-I controls the population and coherence that give rise to the observation of ground or excited state dynamics[5] and this is independent of the detection wavelength. We have confirmed this fact experimentally by collecting three-pulse FWM data as a function of τ_{ab}, τ and the detection wavelength. The results confirm the control mechanism for all detection wavelengths.[11] Minor deviations in the data result from differences between the real molecular system and the four-level model solved using third-order perturbation theory.

The effects caused by chirp in the excitation pulses reflect the characteristics of the potential energy surfaces and the nascent wave packet dynamics. The effects of laser chirp in the excitation of molecular iodine have been studied by various groups.[30–35] Here we have shown with three-pulse FWM that we are able to follow the changes in the dynamics of the system caused by the magnitude and sign of the chirp. These observations are similar to those observed in pump–probe experiments. However, our study showed that the three-pulse FWM signal carries a wealth of

spectral information. When spectrally dispersed three-pulse FWM was used to explore the role of excitation with chirped laser pulses, the data showed a clear change in the amplitude of individual spectroscopic transitions. Negatively chirped pulses enhanced the amplitude of the long-wavelength transitions, while positive chirps enhanced the short-wavelength transitions. The data as a function of τ_{ab}, τ_1 detection wavelength, and chirp show that the pulse sequence controls the population and coherence transfer.[5,11] When beams E_a and E_b are equally chirped, one controls the coherence transfer.[11] A more complete discussion of these experiments will be published elsewhere.[36]

Three-pulse FWM is a multidimensional technique that can yield a wealth of information about the ground and excited state dynamics of molecules. We hope to expand these studies to reactive systems in the near future.

6. Acknowledgements

MD acknowledges the support of this work from the National Science Foundation Grant CHE-9812584. Additional funding comes from a Packard Science and Engineering Fellowship, an Alfred P. Sloan Research Fellowship and a Camille Dreyfus Teacher–Scholar award. EJB is supported by a National Science Foundation Graduate Fellowship.

Appendix A

After applying n electric fields, the density matrix of order n can be obtained from

$$\hat{\rho}^{(n)}(t) = \left(\frac{-\mathrm{i}}{\hbar}\right) \int_{-\infty}^{t} \mathrm{d}t_n \mathscr{G}(t - t_n)[\hat{P}, \hat{\rho}^{(n-1)}(t_n)]E^{(n)}(\boldsymbol{r}, t_n). \tag{A1}$$

In the above equation, the operator $[\hat{P}, \hat{\rho}^{(n-1)}(t_n)]$ is the commutator between the operator $\hat{P}$ and $\hat{\rho}^{(n-1)}(t_n)$,

$$[\hat{P}, \hat{\rho}^{(n-1)}(t_n)] = \hat{P}\hat{\rho}^{(n-1)}(t_n) - \hat{\rho}^{(n-1)}(t_n)\hat{P} \tag{A2}$$

and $\mathscr{G}(t - t_n)$ is Green's operator,[10]

$$\mathscr{G}(t - t_n)\hat{\rho}^{(n-1)}(t_n) = \exp\left\{\frac{\mathrm{i}(t - t_n)}{\hbar}[\hat{H}, \hat{\rho}^{(n-1)}(t_n)]\right\} \tag{A3}$$

where the operator $\hat{H}$ is the unperturbed molecular Hamiltonian. The role of Green's function is to propagate the density matrix in Liouville space during the time between two successive interactions.[10]

The operator $\hat{P}$ is given by the time-independent dipole coupling,

$$\hat{P} = \begin{pmatrix} 0 & \mu_{12} \\ \mu_{21} & 0 \end{pmatrix} \tag{A4}$$

where μ_{ij} are the dipole moments of the transitions. The FWM signal arises only from molecules that have interacted with all three fields; therefore, the third-order density matrix operator, $\hat{\rho}^{(3)}(t)$, is the key to determining the signal (see eqn. (2)).

After the first dipole interaction, $\rho^{(1)}(t)$ can be obtained from eqn. (A1) with $n = 1$ and $t_1 = 0$,

$$\hat{\rho}^{(1)}(t) = \frac{\mathrm{i}}{\hbar}\begin{pmatrix} 0 & -a_{21}\, \mathrm{e}^{\mathrm{i}(\omega_{21}t - \boldsymbol{k}_1 \cdot \boldsymbol{r})} \\ a_{21}\, \mathrm{e}^{-\mathrm{i}(\omega_{21}t - \boldsymbol{k}_1 \cdot \boldsymbol{r})} & 0 \end{pmatrix} \tag{A5}$$

with

$$a_{21} = \mu_{21} \int \tilde{E}^{(1)}(t)\, \mathrm{d}t. \tag{A6}$$

In these expressions, the pulses do not contain any phase modulation and thus $a_{12} = a_{21}^* = a_{21}$. According to the Feynman diagrams, $\hat{\rho}^{(1)}(t)$ is a coherence containing $\rho_{12}^{(1)}(t)$ and $\rho_{21}^{(1)}(t)$. Note that the diagonal elements representing the populations are zero. When the second electric field is

applied with a time delay τ_{ab}, $\hat{\rho}^{(2)}(t)$ is given by,

$$\hat{\rho}^{(2)}(t) = 2\left(\frac{i}{\hbar}\right)^2 \begin{pmatrix} a_{21}b_{12}\cos(\Omega_{21}\tau_{ab} - (\boldsymbol{k}_1 - \boldsymbol{k}_2)\cdot\boldsymbol{r}) & 0 \\ 0 & -a_{21}b_{12}\cos(\Omega_{21}\tau_{ab} - (\boldsymbol{k}_1 - \boldsymbol{k}_2)\cdot\boldsymbol{r}) \end{pmatrix} \quad \text{(A7)}$$

with

$$b_{12} = \mu_{12}\int \tilde{E}^{(2)*}(t)\,dt. \quad \text{(A8)}$$

If the laser pulses do not have any phase modulation, $b_{21} = b_{12}^* = b_{12}$. Notice that the population in the ground and excited states ($\rho_{11}^{(2)}$ and $\rho_{22}^{(2)}$) depends on the product of $\Omega_{21}\tau_{ab}$ and on the transient grating condition ($\boldsymbol{k}_1 - \boldsymbol{k}_2$). The implication of this dependence is that one can choose τ_{ab} to control the magnitude of the populations, albeit not independently.

According to the Feynman diagrams, $\hat{\rho}^{(2)}(t)$ represents a population state; indeed in eqn. (A7) only the diagonal elements are non-zero corresponding to $\rho_{11}^{(2)}$ or $\rho_{22}^{(2)}$. In this particular case of a two-level system, $\hat{\rho}^{(2)}(t)$ is a stationary matrix because each fraction of the sample is in a stationary eigenstate of the unperturbed Hamiltonian. No relaxation has been included. The density matrix in third-order perturbation theory will be obtained after performing the time integral indicated in eqn. (A3) when a third electric field is delayed by time τ with respect to the second field. Then the expression for $\hat{\rho}^{(3)}(t)$ can be separated into two components, each one with different spatial dependency,

$$\hat{\rho}^{(3)}(t) = \hat{\rho}^{(3)}_{\text{VEcho}}(t) + \hat{\rho}^{(3)}_{\text{Echo}}(t) \quad \text{(A9)}$$

where

$$\hat{\rho}^{(3)}_{\text{VEcho}}(t) = 2\left(\frac{i}{\hbar}\right)^3 \begin{pmatrix} 0 & -a_{21}b_{12}c_{21}\,e^{i[\Omega_{21}(t-\tau)-(\boldsymbol{k}_3-\boldsymbol{k}_2+\boldsymbol{k}_1)\cdot\boldsymbol{r}]} \\ a_{21}b_{12}c_{21}\,e^{-i[\Omega_{21}(t-\tau)-(\boldsymbol{k}_3-\boldsymbol{k}_2+\boldsymbol{k}_1)\cdot\boldsymbol{r}]} & 0 \end{pmatrix} \quad \text{(A10a)}$$

and

$$\hat{\rho}^{(3)}_{\text{Echo}}(t) = 2\left(\frac{i}{\hbar}\right)^3 \begin{pmatrix} 0 & -a_{21}b_{12}c_{21}\,e^{i[\Omega_{21}(t-\tau-2\tau_{ab})-(\boldsymbol{k}_3+\boldsymbol{k}_2-\boldsymbol{k}_1)\cdot\boldsymbol{r}]} \\ a_{21}b_{12}c_{21}\,e^{-i[\Omega_{21}(t-\tau-2\tau_{ab})-(\boldsymbol{k}_3+\boldsymbol{k}_2-\boldsymbol{k}_1)\cdot\boldsymbol{r}]} & 0 \end{pmatrix} \quad \text{(A10b)}$$

with

$$c_{21} = \mu_{21}\int \tilde{E}^{(3)}(t)\,dt. \quad \text{(A11)}$$

If the pulses are not chirped, $c_{12} = c_{21}^* = c_{21}$. In order to derive an expression for the signal, we need to calculate the average of the polarization, $P^{(3)}$, according to eqn. (2),

$$P^{(3)}(t) = \mu_{12}\rho_{21}^{(3)}(t) + \mu_{21}\rho_{12}^{(3)}(t) \quad \text{(A12)}$$

which can be separated into two parts based on their spatial directions, *i.e.* phase-matching conditions, as above (eqn. (A9)). In our experimental set-up, we are measuring the signal from the first polarization term in eqn. (A9) where $\boldsymbol{k}_s = \boldsymbol{k}_3 - \boldsymbol{k}_2 + \boldsymbol{k}_1$. The other term has the direction $\boldsymbol{k}_s = \boldsymbol{k}_3 + \boldsymbol{k}_2 - \boldsymbol{k}_1$ and corresponds to a photon echo signal. Therefore, based on the detection geometry, one can measure the signal corresponding to each term separately.

Appendix B

Each component of the density matrix of order n can be obtained from eqn. (A3),

$$\rho_{ij}^{(n)} = -\frac{i}{\hbar}\int_{-\infty}^{t} [\hat{P}, \hat{\rho}^{(n-1)}(t'_n)]_{ij}\, e^{i\omega_{ij}t'_n}E^{(n)}(t - t'_n)\,dt'_n \quad \text{(B1)}$$

or

$$\rho_{ij}^{(n)}(t) = \frac{-\mathrm{i}}{\hbar}\int_{-\infty}^{t} \Sigma[\mu_{im}\rho_{mj}^{(n-1)}(t_n') - \rho_{im}^{(n-1)}(t_n')\mu_{mj}]\mathrm{e}^{\mathrm{i}\Omega_{ij}t_n'}E^{(n)}(t-t_n')\,\mathrm{d}t_n' \tag{B2}$$

where the explicit expression for the ij component of the commutator has been applied. If the pulses are short and do not overlap the upper limit of the time integral can be $t \to \infty$. In that case the solution of the Liouville equation can be simplified as

$$\rho_{ij}^{(n)}(t) = \mathrm{i}\mathrm{e}^{-\mathrm{i}\Omega_{ij}(t-t_n)}\sum_{m=1}^{4}[V_{im}^{(n)}\rho_{mj}^{(n-1)}(t_n) - \rho_{im}^{(n-1)}(t_n)V_{mj}^{(n)}] \tag{B3}$$

where t_n is the time when pulse $E^{(n)}$ is applied and

$$V_{ij}^{(n)} = \tfrac{1}{2}\alpha_{ij}^{(n)}\,\mathrm{e}^{\mathrm{i}(\boldsymbol{k}_n\cdot\boldsymbol{r})} \tag{B4a}$$

where the "area under the pulse" is

$$\alpha_{ij}^{(n)} = \frac{2\mu_{ij}}{\hbar}\int \tilde{E}^{(n)}(t)\mathrm{e}^{\mathrm{i}(\Omega_{ij}-\omega)t}\,\mathrm{d}t \tag{B4b}$$

and μ_{ij} are the dipole moments in the Franck–Condon approximation. After the first pulse is applied, a coherence appears between the different electronic states. These off-diagonal elements are

$$\rho_{31}^{(1)}(t) = \mathrm{i}\,\mathrm{e}^{-\mathrm{i}\Omega_{31}(t)}V_{31}^{(1)}\rho_{11}^{(0)}, \tag{B5a}$$

$$\rho_{32}^{(1)}(t) = \mathrm{i}\,\mathrm{e}^{-\mathrm{i}\Omega_{32}(t)}V_{32}^{(1)}\rho_{22}^{(0)}, \tag{B5b}$$

$$\rho_{41}^{(1)}(t) = \mathrm{i}\,\mathrm{e}^{-\mathrm{i}\Omega_{41}(t)}V_{41}^{(1)}\rho_{11}^{(0)}, \quad \text{and} \tag{B5c}$$

$$\rho_{42}^{(1)}(t) = \mathrm{i}\,\mathrm{e}^{-\mathrm{i}\Omega_{42}(t)}V_{42}^{(1)}\rho_{22}^{(0)}. \tag{B5d}$$

Complex conjugate elements are not shown. Likewise, eqn. (B3) is used to determine the density matrix elements after the second and third field interactions. The virtual echo part of $\hat{\rho}^{(3)}$ is a linear combination of the terms from $V^{(1)}V^{(2)*}V^{(3)}$ and its complex conjugate; it has time and space dependence corresponding to $\mathrm{e}^{-\mathrm{i}(\omega t-(\boldsymbol{k}_3-\boldsymbol{k}_2+\boldsymbol{k}_1)\cdot\boldsymbol{r})}$ and its complex conjugate. The photon echo part is a linear combination of the terms from $V^{(1)*}V^{(2)}V^{(3)}$ and its complex conjugate with time and space dependence given by $\mathrm{e}^{-\mathrm{i}(\omega t-(\boldsymbol{k}_3+\boldsymbol{k}_2-\boldsymbol{k}_1)\cdot\boldsymbol{r})}$ and its complex conjugate. We have solved the general four-level system; however, we have chosen to present only the virtual echo portion that corresponds to the signal we detected. The virtual echo portion of the density matrix will be noted as $\tilde{\rho}_{ij}^{(n)}$.

Since the transitions are resonant and the pulses degenerate, the area under the pulse $\alpha_{ij}^{(n)}$ (eqn. (B4b)), is equal for all order n and ij indices, then $\alpha = |\alpha_{ij}^{(1)}| = |\alpha_{ij}^{(2)}| = |\alpha_{ij}^{(3)}|$. We assume that all transition dipole moments have the same amplitude $\mu = |\mu_{ij}|$ for all i and j. The sign for each transition depends on the relative displacement of the potential energy curves for the two electronic states. When the excited state is shifted to larger internuclear distances, as is the case for molecular iodine, the sign is positive for transitions involving an even vibrational level in the ground state and negative for those involving an odd vibrational level. We define the frequencies between the states as

$$\Omega_{32} = \omega - \tfrac{1}{2}\omega_{\mathrm{g}} - \tfrac{1}{2}\omega_{\mathrm{e}}, \tag{B6a}$$

$$\Omega_{42} = \omega - \tfrac{1}{2}\omega_{\mathrm{g}} + \tfrac{1}{2}\omega_{\mathrm{e}}, \tag{B6b}$$

$$\Omega_{31} = \omega + \tfrac{1}{2}\omega_{\mathrm{g}} - \tfrac{1}{2}\omega_{\mathrm{e}}, \quad \text{and} \tag{B6c}$$

$$\Omega_{41} = \omega + \tfrac{1}{2}\omega_{\mathrm{g}} + \tfrac{1}{2}\omega_{\mathrm{e}}, \tag{B6d}$$

where ω_{g} and ω_{e} are the vibrational frequencies of the ground and excited states and ω is the carrier frequency of the laser.

At the time the third electric field is applied, $t_3 = \tau_{ab} + \tau$, the density matrix elements corresponding to the transient grating phase-matching condition for the ground state are

$$\tilde{\rho}^{(2)}_{11}(t_3) = -\tfrac{1}{2}e^{-i(\omega+(1/2)\omega_g)\tau_{ab}}\cos(\tfrac{1}{2}\omega_e\tau_{ab})\rho^0_{11}\alpha^2\, e^{i(\boldsymbol{k}_1-\boldsymbol{k}_2)\cdot\boldsymbol{r}}, \tag{B7a}$$

$$\tilde{\rho}^{(2)}_{22}(t_3) = -\tfrac{1}{2}e^{-i(\omega-(1/2)\omega_g)\tau_{ab}}\cos(\tfrac{1}{2}\omega_e\tau_{ab})\rho^0_{22}\alpha^2\, e^{i(\boldsymbol{k}_1-\boldsymbol{k}_2)\cdot\boldsymbol{r}}, \tag{B7b}$$

$$\tilde{\rho}^{(2)}_{12}(t_3) = \tfrac{1}{2}e^{i\omega_g\tau}\, e^{-i(\omega-(1/2)\omega_g)\tau_{ab}}\cos(\tfrac{1}{2}\omega_e\tau_{ab})\rho^0_{22}\alpha^2\, e^{i(\boldsymbol{k}_1-\boldsymbol{k}_2)\cdot\boldsymbol{r}}, \quad \text{and} \tag{B7c}$$

$$\tilde{\rho}^{(2)}_{21}(t_3) = \tfrac{1}{2}e^{-i\omega_g\tau}\, e^{-i(\omega+(1/2)\omega_g)\tau_{ab}}\cos(\tfrac{1}{2}\omega_e\tau_{ab})\rho^0_{11}\alpha^2\, e^{i(\boldsymbol{k}_1-\boldsymbol{k}_2)\cdot\boldsymbol{r}}, \tag{B7d}$$

where eqns. (B6a)–(B6d) were used to reduce the Ω_{ij} to the vibrational frequencies of the ground and excited states, ω_g and ω_e. The corresponding density matrix elements for the excited state are

$$\tilde{\rho}^{(2)}_{33}(t_3) = \tfrac{1}{4}(e^{-i\omega_g\tau_{ab}/2}\rho^0_{11} + e^{i\omega_g\tau_{ab}/2}\rho^0_{22})e^{i\omega_e\tau_{ab}/2}\alpha^2\, e^{-i(\omega\tau_{ab}-(\boldsymbol{k}_1-\boldsymbol{k}_2)\cdot\boldsymbol{r})}, \tag{B8a}$$

$$\tilde{\rho}^{(2)}_{44}(t_3) = \tfrac{1}{4}(e^{-i\omega_g\tau_{ab}/2}\rho^0_{11} + e^{i\omega_g\tau_{ab}/2}\rho^0_{22})e^{-i\omega_e\tau_{ab}/2}\alpha^2\, e^{-i(\omega\tau_{ab}-(\boldsymbol{k}_1-\boldsymbol{k}_2)\cdot\boldsymbol{r})}, \tag{B8b}$$

$$\tilde{\rho}^{(2)}_{34}(t_3) = \tfrac{1}{4}e^{i\omega_e\tau}(e^{-i\omega_g\tau_{ab}/2}\rho^0_{11} + e^{i\omega_g\tau_{ab}/2}\rho^0_{22})e^{i\omega_e\tau_{ab}/2}\alpha^2\, e^{-i(\omega\tau_{ab}-(\boldsymbol{k}_1-\boldsymbol{k}_2)\cdot\boldsymbol{r})}, \quad \text{and} \tag{B8c}$$

$$\tilde{\rho}^{(2)}_{4}(t_3) = \tfrac{1}{4}e^{i\omega_e\tau}(e^{-i\omega_g\tau_{ab}/2}\rho^0_{11} + e^{i\omega_g\tau_{ab}/2}\rho^0_{22})e^{i\omega_e\tau_{ab}/2}\alpha^2\, e^{-i(\omega\tau_{ab}-(\boldsymbol{k}_1-\boldsymbol{k}_2)\cdot\boldsymbol{r})}. \tag{B8d}$$

These equations cannot be put in terms of ω_e and ω_g because this would require knowing the initial state of the system. If we define this initial population distribution by $w = \rho^0_{11} - \rho^0_{22}$, we can see that eqns. (B8a)–(B8d) can be simplified for $w = 0$ or $w = 1$. To simplify eqns. (B8a)–(B8d) when $w = 0$, interchange ω_g and ω_e in eqns. (B7a)–(B7d) to obtain the corrresponding equations for the excited state components. The general solution for this is given when we analyze the signal. After applying the third pulse and pulling out only the terms with the correct phase-matching condition, we obtain

$$\tilde{\rho}^{(3)}_{31}(t) = \tfrac{1}{2}i\, e^{-i\omega_{31}(t-t_3)}\{[\tilde{\rho}^{(2)}_{11}(t_3) - \tilde{\rho}^{(2)}_{21}(t_3)] - [\tilde{\rho}^{(2)}_{33}(t_3) + \tilde{\rho}^{(2)}_{34}(t_3)]\}\alpha\, e^{i\boldsymbol{k}_3\cdot\boldsymbol{r}}, \tag{B9a}$$

$$\tilde{\rho}^{(3)}_{32}(t) = \tfrac{1}{2}i\, e^{-i\omega_{32}(t-t_3)}\{[\tilde{\rho}^{(2)}_{12}(t_3) - \tilde{\rho}^{(2)}_{22}(t_3)] + [\tilde{\rho}^{(2)}_{33}(t_3) + \tilde{\rho}^{(2)}_{34}(t_3)]\}\alpha\, e^{i\boldsymbol{k}_3\cdot\boldsymbol{r}}, \tag{B9b}$$

$$\tilde{\rho}^{(3)}_{41}(t) = \tfrac{1}{2}i\, e^{-i\omega_{41}(t-t_3)}\{[\tilde{\rho}^{(2)}_{11}(t_3) - \tilde{\rho}^{(2)}_{21}(t_3)] - [\tilde{\rho}^{(2)}_{43}(t_3) + \tilde{\rho}^{(2)}_{44}(t_3)]\}\alpha\, e^{i\boldsymbol{k}_3\cdot\boldsymbol{r}}, \quad \text{and} \tag{B9c}$$

$$\tilde{\rho}^{(3)}_{42}(t) = \tfrac{1}{2}i\, e^{-i\omega_{42}(t-t_3)}\{[\tilde{\rho}^{(2)}_{12}(t_3) - \tilde{\rho}^{(2)}_{22}(t_3)] + [\tilde{\rho}^{(2)}_{43}(t_3) + \tilde{\rho}^{(2)}_{44}(t_3)]\}\alpha\, e^{i\boldsymbol{k}_3\cdot\boldsymbol{r}}. \tag{B9d}$$

Note that the first term in the braces in eqns. (B9a)–(B9d) corresponds to ground state contribution and the second term to excited state. Therefore, by applying eqn. (2), we can separate the polarization into components having a time dependence modulated at the ground or excited state vibrational frequency, P_g and P_e, respectively. This separation was carried out by expanding each $\tilde{\rho}^{(2)}_{ij}$ term and grouping similar terms according to those that contain a $\cos(\frac{1}{2}\omega_g\tau)$ or $\cos(\frac{1}{2}\omega_e\tau)$ factor.

References

1 S. A. Passino, Y. Nagasawa and G. R. Fleming, *J. Chem. Phys.*, 1997, **107**, 6094.
2 W. P. de Boeij, M. S. Pshenichnikov and D. A. Wiersma, *Annu. Rev. Phys. Chem.*, 1998, **49**, 99.
3 M. N. Yang and G. R. Fleming, *J. Chem. Phys.*, 1999, **110**, 2983.
4 Y. J. Yan, L. E. Fried and S. Mukamel, *J. Phys. Chem.*, 1989, **93**, 8149.
5 E. J. Brown, I. Pastirk, B. I. Grimberg, V. V. Lozovoy and M. Dantus, *J. Chem. Phys.*, accepted.
6 R. J. Gordon and S. A. Rice, *Annu. Rev. Phys. Chem.*, 1997, **48**, 601.
7 P. Gaspard and I. Burghardt, in *Chemical Reactions and Their Control on the Femtosecond Timescale*, Wiley, New York, 1997.
8 A. Assion, T. Baumert, M. Bergt, T. Brixner, B. Kiefer, V. Seyfried, M. Strehle and G. Gerber, *Science*, 1998, **282**, 919.
9 Y. R. Shen, *The Principle of Nonlinear Optics*, Wiley, New York, 1984.
10 S. Mukamel, *Principles of Nonlinear Optical Spectroscopy*, Oxford University Press, New York, 1995, ch. 5.
11 I. Pastirk, V. V. Lozovoy, I. Grimberg, E. J. Brown and M. Dantus, *J. Phys. Chem. A*, submitted.
12 E. J. Brown, Q. Zhang and M. Dantus, *J. Chem. Phys.*, 1999, **110**, 5772.
13 V. V. Lozovoy, I. Pastirk, E. J. Brown, B. I. Grimberg and M. Dantus, in preparation.

14 P. H. Vaccaro, in *Degenerate Four-Wave Mixing* (*DFWM*) *Spectroscopy*, ed. E. Hirota, R. W. Field, J. P. Maier and S. Tsuchiya, Blackwell Scientific Publications Ltd. for Physical Chemistry Division of IUPAC, London, 1997.
15 S. Mukamel, M. Cho and G. R. Fleming, *J. Chem. Phys.*, 1993, **98**, 5314.
16 R. W. Boyd, *Nonlinear Optics*, Academic Press, San Diego, 1992.
17 M. S. Pshenichnikov, W. P. d. Boeij and D. A. Wiersma, *Phys. Rev. Lett.*, 1996, **76**, 4701.
18 Y. Prior, *Appl. Opt.*, 1980, **19**, 1741.
19 J. A. Shirley, R. J. Hall and A. C. Eckbreth, *Opt. Lett.*, 1980, **5**, 380.
20 M. Schmitt, G. Knopp, A. Materny and W. Kiefer, *Chem. Phys. Lett.*, 1997, **270**, 9.
21 M. Schmitt, G. Knopp, A. Materny and W. Kiefer, *Chem. Phys. Lett.*, 1997, **280**, 339.
22 S. Meyer, M. Schmitt, A. Materny, W. Kiefer and V. Engel, *Chem. Phys. Lett.*, 1999, **301**, 248.
23 J. Tellinghuisen, *J. Quant. Spectrosc. Radiat. Transfer*, 1978, **19**, 149.
24 M. Dantus, R. M. Bowman and A. H. Zewail, *Nature* (*London*), 1990, **343**, 737.
25 M. Gruebele, G. Roberts, M. Dantus, R. M. Bowman and A. H. Zewail, *Chem. Phys. Lett.*, 1990, **166**, 459.
26 R. J. LeRoy, *J. Chem. Phys.*, 1970, **52**, 2683.
27 V. V. Lozovoy, I. Pastirk and M. Dantus, *J. Chem. Phys.*, submitted.
28 W. M. Zhang, V. Chernyak and S. Mukamel, *J. Chem. Phys.*, 1999, **110**, 5011.
29 T.-S. Yang, R. Zhang and A. Myers, *J. Chem. Phys.*, 1994, **100**, 8573.
30 M. Sterling, R. Zadoyan and V. A. Apkarian, *J. Chem. Phys.*, 1996, **104**, 6497.
31 C. J. Bardeen, J. Che, K. R. Wilson, V. Yakovlev, V. A. Apkarian, C. C. Martens, R. Zadoyan, B. Kohler and M. Messin, *J. Chem. Phys.*, 1997, **106**, 8486.
32 V. Yakovlev, C. J. Bardeen, J. Che, J. Cao and K. R. Wilson, *J. Chem. Phys.*, 1998, **108**, 2309.
33 V. V. Lozovoy, S. A. Antipin, F. E. Gostev, A. A. Titov, D. G. Tovbin, O. M. Sarkisov, A. S. Vetchinkin and S. Y. Umanskii, *Chem. Phys. Lett.*, 1998, **284**, 221.
34 V. V. Lozovoy, A. A. Titov, F. E. Gostev, D. G. Tovbin, S. A. Antipin, S. Y. Umanskii and O. M. Sarkisov, *Chem. Phys. Rep.* 1998, **17**, 1267.
35 V. V. Lozovoy, O. M. Sarkisov, A. S. Vetchinkin and S. Y. Umanskii, *Chem. Phys.*, 1999, **243**, 97.
36 B. I. Grimberg, V. V. Lozovoy and M. Dantus, in preparation.
37 B. Broers, H. B. van Linden van den Heuvell and L. D. Noordam, *Phys. Rev. Lett.*, 1992, **69**, 2062.
38 J. S. Melinger, S. R. Gandhi, A. Hariharan, J. X. Tull and W. S. Warren, *Phys. Rev. Lett.*, 1992, **68**, 2000.
39 J. S. Melinger, S. R. Gandhi, A. Hariharan, D. Goswami and W. S. Warren, *J. Chem. Phys.*, 1994, **101**, 6439.
40 Y. B. Band and O. Magnes, *Phys. Rev. A*. 1994, **50**, 584.
41 N. F. Scherer, A. J. Ruggiero, M. Du and G. R. Fleming, *J. Chem. Phys.*, 1990, **93**, 856.

Paper 9/02571E